

REPORT DOCUMENTATION PAGE			Form Approved OMB NO. 0704-0188		
<p>The public reporting burden for this collection of information is estimated to average 1 hour per response, including the time for reviewing instructions, searching existing data sources, gathering and maintaining the data needed, and completing and reviewing the collection of information. Send comments regarding this burden estimate or any other aspect of this collection of information, including suggestions for reducing this burden, to Washington Headquarters Services, Directorate for Information Operations and Reports, 1215 Jefferson Davis Highway, Suite 1204, Arlington VA, 22202-4302. Respondents should be aware that notwithstanding any other provision of law, no person shall be subject to any penalty for failing to comply with a collection of information if it does not display a currently valid OMB control number. PLEASE DO NOT RETURN YOUR FORM TO THE ABOVE ADDRESS.</p>					
1. REPORT DATE (DD-MM-YYYY) 31-08-2015		2. REPORT TYPE Ph.D. Dissertation		3. DATES COVERED (From - To) -	
4. TITLE AND SUBTITLE Light-Assisted, Templated Self Assembly Using Photonic Crystal Slabs			5a. CONTRACT NUMBER W911NF-09-1-0473		
			5b. GRANT NUMBER		
			5c. PROGRAM ELEMENT NUMBER 611102		
6. AUTHORS Eric Jaquay			5d. PROJECT NUMBER		
			5e. TASK NUMBER		
			5f. WORK UNIT NUMBER		
7. PERFORMING ORGANIZATION NAMES AND ADDRESSES University of Southern California Dept of Contracts and Grants University of Southern California Marina del Rey, CA 90292 -6601			8. PERFORMING ORGANIZATION REPORT NUMBER		
9. SPONSORING/MONITORING AGENCY NAME(S) AND ADDRESS (ES) U.S. Army Research Office P.O. Box 12211 Research Triangle Park, NC 27709-2211			10. SPONSOR/MONITOR'S ACRONYM(S) ARO		
			11. SPONSOR/MONITOR'S REPORT NUMBER(S) 56801-MS-PCS.19		
12. DISTRIBUTION AVAILABILITY STATEMENT Approved for public release; distribution is unlimited.					
13. SUPPLEMENTARY NOTES The views, opinions and/or findings contained in this report are those of the author(s) and should not be construed as an official Department of the Army position, policy or decision, unless so designated by other documentation.					
14. ABSTRACT In this thesis we have successfully demonstrated the technique that we call light-assisted, templated self assembly. In the first demonstration we successfully trapped an array of 520 nm polystyrene particles above a square lattice. The number of particles trapped was well above 100, and could be increased by using a larger beam or a mode with a larger quality factor. The traps were characterized using standard techniques and were found to have stiffness values comparable to those reported elsewhere in the literature for single-particle traps. The system behaved as an array of non-interacting optical traps, with each trap positioned above the hole in each unit cell of the square lattice.					
15. SUBJECT TERMS optical trapping, self assembly, optical forces, nanoparticles					
16. SECURITY CLASSIFICATION OF:		17. LIMITATION OF ABSTRACT	15. NUMBER OF PAGES	19a. NAME OF RESPONSIBLE PERSON	
a. REPORT	b. ABSTRACT			c. THIS PAGE	Michelle Povinelli
UU	UU	UU		19b. TELEPHONE NUMBER	
				213-740-8682	

Report Title

Light-Assisted, Templated Self Assembly Using Photonic Crystal Slabs

ABSTRACT

In this thesis we have successfully demonstrated the technique that we call light-assisted, templated self assembly. In the first demonstration we successfully trapped an array of 520 nm polystyrene particles above a square lattice. The number of particles trapped was well above 100, and could be increased by using a larger beam or a mode with a larger quality factor. The traps were characterized using standard techniques and were found to have stiffness values comparable to those reported elsewhere in the literature for single-particle traps. The system behaved as an array of non-interacting optical traps, with each trap positioned above the hole in each unit cell of the square lattice. Although other techniques exist for trapping arrays of particles, they typically require a spatial light modulator and fast-scanning mirrors. Our technique requires just a simple, Gaussian input beam.

Next we repeated the LATS technique but with metallic particles. Our expectation was that the technique would either work – namely that we would trap an array of the metallic particles – or it would not work. Instead, we found an intermediate case involving the emergence of one-dimensional particle chains trapped in a two-dimensionally periodic potential due to the mode in the slab. The chains were observed to align in the direction opposite to the incident polarization of the beam. The particles in chains were self-stabilizing in the sense that these particles persisted much longer than other particles that were trapped in isolated positions. We explained these results by using a simplified model of the particle scattering in the absence of the slab. The system is best understood as a competition between particle-template and particle-particle interactions.

Light-Assisted, Templated Self Assembly Using Photonic Crystal Slabs

A Dissertation submitted to the faculty of the graduate school

University of Southern California

In partial fulfillment of the requirements for the degree of
Doctor of Philosophy

Eric Andrew Jaquay

October 2014

Copyright Eric Jaquay 2014

Acknowledgments

I'd like to thank my advisor, Dr. Michelle Povinelli, for her guidance and support throughout my time at USC. I'd also like to thank the various labmates I had throughout the years. Chenxi Lin, Jing "Maggie" Ma and I started together and worked hard to make the lab into a functional and friendly environment. Chenxi and I had many disagreements about pronunciation, the definition of soup, and really just about any other topic that we discussed. Maggie was very good at programming and shopping. We were joined after one year by Camilo Mejia, who not only wrote the code for calculating optical forces that we still use, but also ensured that our group meetings were lively. Our postdocs, Mehmet Solmaz and Luis Martínez, brought the first true experimental know-how to the lab. Mehmet filled up the lab with all the stuff a good optical laboratory needs. Luis in particular was instrumental in my success, and I feel lucky to have interacted with such a singularity of humanity. I also owe a debt of gratitude and friendship to Roshni Biswas, who seems to be following the same academic pace as I was; Ningfeng Huang, who is perhaps the smartest member the lab has known or will ever know; Duke Anderson, who is always good for a laugh or two; Shao-Hua Wu, who is a diligent worker and will have great success; and Aravind Krishnan, who has been around for just a few months but already fits in well. I'd also like to thank the following USC students who helped me gain my footing in my early days: Larry Stewart, Raymond Sarkissian, Chuan Wang, Peichi Hu, and Mir-Ashkan Seyedi. I'd also like to thank Donghai Zhu for his conscientious attention to the maintenance of the aging (and aged) equipment in the clean room. Lastly, I'd like to thank HPCC and its staff for computational resources, without which the calculations in this paper would not be possible.

Table of Contents

Chapter 1 – Introduction	7
1.1 – Radiation Pressure and Optical Trapping	7
1.2 – Near-Field Trapping and Trapping of Multiple Particles	8
1.3 – Theory of Optical Forces	10
1.4 – Non-Optical Forces	12
1.5 – Trap Stiffness	14
1.6 – Self Assembly	14
1.7 – Fabrication	16
1.8 – Experimental Set-up	19
Chapter 2 – Light-Assisted, Templated Self-Assembly of Dielectric Particles	22
2.1 – Introduction.....	22
2.2 – Device Design	24
2.3 – Results	25
2.4 – Simulations	28
2.5 – Discussion	31
2.6 – Methods	32
Chapter 3 – Light-Assisted, Templated Self-Assembly of Metallic Particles	35

3.1 – Introduction.....	35
3.2 – Device Design	36
3.3 – Results	39
3.4 – Simulations	45
3.5 – Discussion	49
3.6 – Methods	49
Chapter 4 – Optical Brownian Ratchet.....	51
4.1 – Introduction.....	51
4.2 – Device Design	53
4.3 – Force and Potential Calculations.....	53
4.4 – Device Re-design	58
Chapter 5 – Future Work	60
5.1 – Assembly of a regular array of metallic particles	60
5.2 – Solidification of assembled arrays	62
Chapter 6 – Conclusion.....	63
References	65

List of Figures

1. A self-assembled array of SiO ₂ spheres on a silicon substrate.	15
2. Schematic view of fabrication recipe.	17
3. Samples fabricated using pseudo-Bosch etching recipe developed for use in the USC clean room.....	18
4. Sample mounted on 1-inch glass slides, immersed in particle solution, and sealed with PDMS chamber on glass.	19
5. Schematic of experimental set-up used to characterize samples and perform assembly experiments.	21
6. Schematic of light-assisted, templated self assembly (LATS).....	23
7. Square lattice photonic crystal.	25
8. Light-assisted, templated self assembly of 520 nm diameter particles above a photonic crystal slab.....	26
9. Trap stiffness for incident, <i>x</i> -polarized light.....	27
10. Calculated optical forces using the Maxwell stress tensor method.....	29
11. In-plane optical potential map in one unit cell.....	30
12. Schematic view of light-assisted, templated self assembly (LATS) of gold nanoparticles	36
13. Silicon photonic crystal device	38
14. Assembly of nanoparticle chains.....	40
15. Chain formation as a function of polarization angle	42
16. Stability of trapped particles	44
17. Forces calculated via the Maxwell stress tensor method in dimensionless units of F_c/P .46	
18. Potential energy surfaces for 200 nm diameter Au particles in water, illuminated by a plane wave with a vacuum wavelength of 1550 nm.....	47

19. Schematic of “on-off Brownian ratchet.”	51
20. 3x3 array of asymmetric unit cells in a photonic crystal lattice	52
21. Photonic crystal rectangular lattice with asymmetric unit cell	53
22. Forces and potential for the mode labeled “b” in Figure 21	55
23. Probability of net motion as a function of τ_{off}	56
24. Ratchet device characterization.....	57
25. Redesign of ratchet device	58
26. Device for assembly of 2D nanoparticle array.....	61
27. Assembly of a 2D array of 200 nm Au particles.....	61

Chapter 1 – Introduction

1.1 – Radiation Pressure and Optical Trapping

Kepler first proposed the concept of radiation pressure in 1619 to explain the observation that comets' tails pointed away from the sun at all points along their paths [1]. The notion that electromagnetic radiation could exert mechanical forces on objects in its path was re-introduced by Maxwell in 1862 as part of his electrodynamic theory of light [2]. The first laboratory demonstrations of these effects were performed independently by Lebedev [3] and Nichols and Hull [4, 5] in 1901. These effects were seen as quite weak and required sophisticated equipment to detect at the time, and it was not clear that this discovery would lead to widespread uses.

It wasn't until after the invention of the laser that radiation pressure found practical applications. In 1986 Ashkin demonstrated that a single, tightly-focused laser beam could be used to stably trap neutral dielectric particles in three dimensions [6]. In subsequent work Ashkin showed that the same technique could be applied to the manipulation of cells [7]. The technique enables the manipulation of small objects without physical contact and, provided that incident power is low, without damage to the specimen. These so-called optical tweezers have become indispensable in the fields of biology and physics. They have been used to trap a variety of objects, including not only dielectric particles and living cells, but also metal particles [8-15], strands of DNA [16, 17], bacteria [18], etc. Carefully calibrated optical tweezers have been used to illuminate the intracellular mechanical action of molecular motors [19, 20]. In the field of quantum physics, laser cooling of atoms has enabled scientists to study objects near the quantum ground state. Researchers have been able to extend the cooling technique to the macroscale by cooling a 1 gram object to 0.8 K [21]. A more recent work used laser cooling to bring a nanomechanical oscillator to its quantum ground state [22].

1.2 – Near-Field Trapping and Trapping of Multiple Particles

More recent optical trapping experiments have shown that the evanescent field near microphotonic devices can be used for optical manipulation. The first demonstration of this effect was performed in 1992 by Kawata and Sugiura [23], who showed that objects ranging in size from 1 to 27 μm were attracted toward and propelled along the surface of a prism. Total internal reflection at the surface created a strong gradient in intensity just beyond the surface due to the rapid decay of the evanescent field. A similar demonstration was performed a few years later with a channel waveguide instead of a prism [24]. Device operation and results were much the same. Other authors have demonstrated precise trapping and manipulation of nanoparticles using evanescent fields in a variety of structures [25-27].

More recently, advances in nanofabrication techniques have allowed researchers to trap and transport ever smaller particles using slot waveguides [28], photonic crystal cavities [29-33], and microring resonators [34, 35]. The length over which the evanescent field decays depends upon the index contrast between the device and the surrounding medium. For a silicon device ($n = 3.45$) in an aqueous medium ($n = 1.33$), this decay length is usually confined to 100 nm or less [36]. This strong gradient in intensity near the device surface creates an optical trapping region much smaller than free-space optical traps, whose lateral extents are limited by diffraction.

The optical trapping techniques discussed above are largely designed to operate on single particles. Research has also been done to explore the trapping and manipulation of multiple particles. These techniques can be divided into two main categories. The first category uses time-sharing of a single beam to rapidly displace the trap in space at a time scale shorter than the scale at which the particle diffuses away from the trap [37-40]. This technique involves the use of piezoelectrically-activated stages with mirrors and/or objectives that are scanned across a

predetermined path, or acousto-optic deflectors for higher speed operations. The second category uses spatial light modulators or other diffractive optical elements to generate a static optical potential profile with multiple spatially distinct traps [41-48]. These so-called holographic optical tweezers provide stable traps but also require bulky optics to generate the trapping fields, and as such are poor candidates for system-level miniaturization.

When multiple particles are illuminated uniformly, the field experienced by any one of the particles is a combination of the incident field and the field scattered by other particles. This second effect is often relatively weak, although it can play a significant role in systems with sufficiently intense incident fields, or with sufficiently strong scatterers, e.g. metal particles. Burns *et al.* used these so-called optical binding forces to assemble dielectric particles into “optical matter” – arrays of extended, crystalline structures that were bound together by light [49, 50]. Subsequent work explored these interparticle interactions further. Tatarkova *et al.* used an optical potential well formed via counter-propagating Gaussian beams to explore the dynamics of 1D chains of optically bound particles [51]. A variety of works explored the formation of arrays using counterpropagating light beams in a prism for enhancing interparticle interactions [52-55]. In recent work it was shown that the optical binding forces on 200 nm metal nanoparticles could be as large as 20 times the gradient force for a given geometry featuring an optical line trap near a highly reflective surface [56]. Although previously thought to be much weaker than the gradient force, in [56] it was shown that, in a particular geometry which increased reflections, and with strongly-scattering (i.e. metallic) particles, this optical binding effect was comparable in magnitude to the gradient force.

1.3 – Theory of Optical Forces

Optical forces result whenever electromagnetic radiation interacts with a material. These interactions are governed by Maxwell's equations shown below:

$$\nabla \times \mathbf{E} = -\frac{\partial \mathbf{B}}{\partial t}$$

$$\nabla \times \mathbf{H} = -\frac{\partial \mathbf{D}}{\partial t} + \mathbf{J}$$

$$\nabla \cdot \mathbf{D} = \rho$$

$$\nabla \cdot \mathbf{B} = 0$$

where \mathbf{E} is the electric field, \mathbf{D} is the electric displacement field, \mathbf{H} is the magnetic field, \mathbf{B} is the magnetic induction field, \mathbf{J} is the current density, ρ is the charge density, ϵ is the permittivity of the material and μ is its permeability. The interaction between light and a medium is governed by the constitutive relations:

$$\mathbf{D} = \epsilon \mathbf{E} = \epsilon_0 \epsilon_r \mathbf{E} = \epsilon_0 \mathbf{E} + \mathbf{P}$$

$$\mathbf{B} = \mu \mathbf{H} = \mu_0 \mu_r \mathbf{H}$$

where $\epsilon_0 = 8.854 \times 10^{-12}$ F/m and $\mu_0 = 4\pi \times 10^{-7}$ H/m are constants representing the permittivity and permeability of free space, ϵ_r and μ_r represent the relative permittivity and relative permeability of the medium, and \mathbf{P} is the polarization charge density.

A small test charge q in an electric field \mathbf{E} experiences an electric force $\mathbf{F}_e = q\mathbf{E}$. If the charge is moving with a velocity \mathbf{v} in a magnetic field \mathbf{B} , it also experiences a magnetic force $\mathbf{F}_m = q(\mathbf{v} \times \mathbf{B})$. The total electromagnetic force on this charge, called the Lorentz force, is thus written as

$$\mathbf{F} = q(\mathbf{E} + \mathbf{v} \times \mathbf{B}).$$

Considering some volume of space with charge density ρ and current density \mathbf{J} , this can be re-written as $\mathbf{F} = \rho\mathbf{E} + \mathbf{J} \times \mathbf{B}$. It can be shown that this expression can be re-arranged in the following form:

$$\mathbf{F} = \int \mathbf{T} \cdot \mathbf{n} dS$$

where

$$T_{ij} = \epsilon_0 \epsilon_r E_i E_j + \mu_0 \mu_r H_i H_j - \frac{1}{2} \delta_{ij} (\epsilon_0 \epsilon_r E_k E_k + \mu_0 \mu_r H_k H_k)$$

is an element of a rank-two tensor \mathbf{T} called the Maxwell stress tensor, \mathbf{n} is the unit normal in some closed region of space S over which the integration is performed, and $\{i,j,k\}=\{x,y,z\}$. [57]

The Maxwell stress tensor method can be used to calculate the forces on particles of any size in response to an electromagnetic field. Although this solution is exact for all particle size regimes, it is sometimes easier to work with approximations. In the Rayleigh regime ($a \ll \lambda$, where a is some characteristic length scale of the particle and λ is the wavelength of the light), the dipole approximation can be used. Briefly, the dipole approximation is based on the assumption that the particle is uniformly polarized by the electric field of the external wave into a dipole aligned with the electric field's direction.

In this regime, optical forces can be decomposed into three components: gradient, scattering, and absorption [8, 58, 59]. In general the scattering and absorption forces point in the direction of the propagation of the light, whereas the gradient force points in the direction of the intensity gradient of the light. Successful trapping requires the gradient force to counterbalance the effects of scattering and absorption. (Other forces may be relevant in a given trapping system and will be discussed below.) The gradient force experienced by the particle can be simply written as

$$\mathbf{F}_{\text{grad}} = \frac{|\alpha|}{2} \nabla E^2$$

where $\alpha = 4\pi\epsilon_0 a^3 \frac{\epsilon-1}{\epsilon+2}$ is the polarizability of the particle with radius a . The scattering and absorption forces can be written as

$$\mathbf{F}_{\text{scat}} = \frac{n_m}{c} \sigma_{\text{scat}} \langle \mathbf{S} \rangle$$

$$\mathbf{F}_{\text{abs}} = \frac{n_m}{c} \sigma_{\text{abs}} \langle \mathbf{S} \rangle$$

where n_m is the refractive index of the medium surrounding the particle, $\sigma_{\text{scat}} = \frac{k_m^4 |\alpha|^2}{4\pi}$ is the scattering cross section of the particle, $\sigma_{\text{abs}} = k_m \text{Im}(\alpha)$ is the absorption cross section of the particle, k_m is the wavevector of the light in the medium surrounding the particle, and $\langle \mathbf{S} \rangle$ is the time-averaged Poynting vector of the incident wave.[58, 59] This is often a much simpler and less computationally intensive calculation than the full Maxwell stress tensor method.

1.4 – Non-Optical Forces

There are a variety of non-optical forces that play a role in optical trapping experiments. Typical trapping experiments are performed particles in an aqueous medium, and thus the drag force plays an important role. The drag force is expressed as

$$\mathbf{F}_{\text{drag}} = -\gamma \mathbf{v} = -6\pi\eta a \mathbf{v}$$

where γ is the Stokes drag coefficient, η is the viscosity of the medium, and \mathbf{v} is the relative velocity between the medium and the particle. This expression holds for spherical particles of radius a in a uniform medium. However, the presence of a surface can alter the drag dynamics, via Faxen's Law:

$$\gamma = \frac{6\pi\eta a}{1 - \frac{9}{16} \left(\frac{a}{h}\right) + \frac{1}{8} \left(\frac{a}{h}\right)^3 - \frac{45}{256} \left(\frac{a}{h}\right)^4 - \frac{1}{16} \left(\frac{a}{h}\right)^5}$$

where h is the distance between the center of the particle and the surface. When the particle is in contact with the surface, i.e. $\frac{a}{h} = 1$, the drag coefficient is increased by a factor of 3.[58-60]

The Reynolds number is a dimensionless quantity used to quantify the ratio in a fluidic system between the inertial effects and the viscous effects.[58, 61] This number describes different flow regimes, and is written as

$$Re = \frac{\frac{\rho v^2}{a}}{\frac{\eta v}{a^2}} = \frac{av\rho}{\eta}$$

where ρ is the density of the fluid and all other parameters are as described previously. When the Reynolds number is less than 1000, the system is said to be in the laminar flow regime in which inertial effects are negligible. A particle's velocity is a function of the forces acting on it in that instant, and does not depend on its previous state. Said another way, a particle reaches its terminal velocity instantaneously upon application of a force. For the specific cases of a 520 nm polystyrene particle in water, or a 200 nm gold particle in water, the Reynolds number of our system is less than 1 as long as the particles does not travel at speeds above 1 mm/s.

At wavelengths near 1550 nm, the absorption in the water is significant. The absorption coefficient is near 12 cm^{-1} in this wavelength regime [62], and the resulting heat in the water can lead to thermal effects acting upon particles in solution. These effects may destabilize optical traps using near IR illumination and thus need to be carefully considered. In general the tendency is for particles in solution to move from warm regions to cold regions, although the fluid's convective velocity can be minimized by using a shallow chamber [63].

There are also forces due to gravity, Brownian motion, and van der Waals effects, but these are all several orders of magnitude smaller than the above-mentioned effects and can therefore be neglected.

1.5 – Trap Stiffness

The strength of an optical trap is usually characterized by its stiffness, denoted as κ , which is the first derivative of the force with respect to position ($\kappa = \frac{d\mathbf{F}}{dr}$). The potential generated in an optical trap is well approximated as a harmonic potential, and thus the restoring force is linear: $F = -\kappa r$ for small displacements away from the trap center. The potential energy stored due to a displacement x is thus $\frac{1}{2}\kappa x^2$, in analogy with Hooke's Law, and this fact is often used in an experiment to determine the stiffness of a real trap using the equipartition theorem, which states that the energy in a system is shared equally among its degrees of freedom. In the case of a particle moving in three dimensions, the total kinetic energy is $\frac{3}{2}k_B T$, or $\frac{1}{2}k_B T$ in each dimension (k_B is Boltzmann's constant, and T is temperature). Thus for thermally-induced linear displacements away from a trap center, $\kappa = \frac{k_B T}{\langle x^2 \rangle}$, where $\langle x^2 \rangle$ is the time-averaged variance of observed particle positions away from the center of a trap, and can be extracted from a video of the trapping experiment.

1.6 – Self Assembly

Self-assembly methods [64] have been used to construct complex three-dimensional nanostructures such as photonic crystals [65, 66]. In [67] the authors used the tendency of sub-micron spheres to spontaneously organize into regular, ordered arrays. After a 3D array was assembled (see Fig. 1), silicon was infiltrated into the array, and then the template (i.e. the array of spheres) was dissolved. By carefully choosing the size of the spheres, they were able to fabricate a lattice on a silicon platform that had a band gap in the communications wavelength range. Such a bottom-up technique for fabricating optical devices was expected to enable a variety of novel applications.

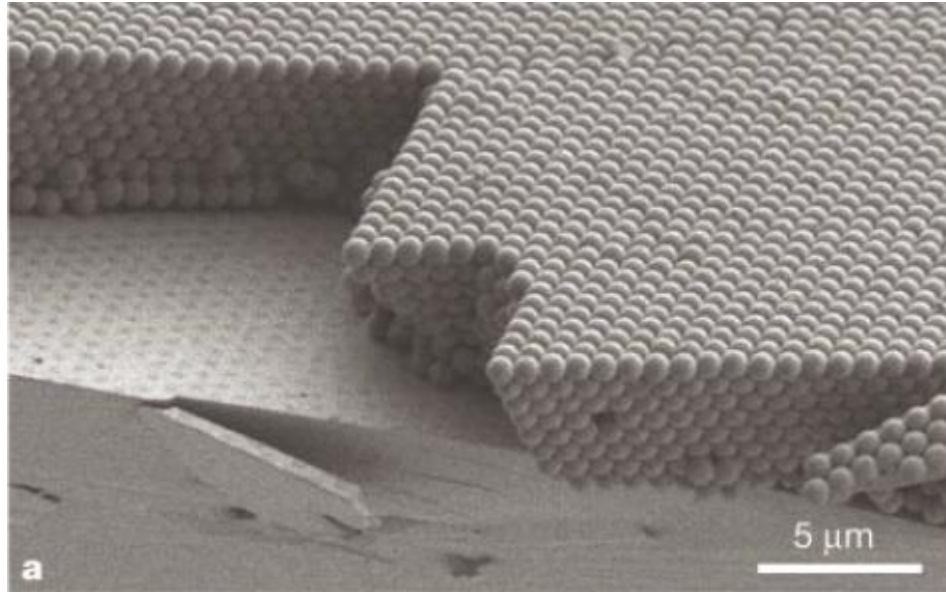


Figure 1. From reference [66]. A self-assembled array of SiO₂ spheres on a silicon substrate.

The most energetically favorable arrangement of nanoparticles is a closely-packed structure with hexagonal symmetry (i.e. face-centered cubic or fcc lattice). A self-assembled fcc lattice of silica spheres is shown in Fig. 1. This geometrical constraint limits the structures that can be formed using self-assembly, and ultimately the material properties of the resulting structures. To overcome this limitation, various methods for directing self-assembly have been proposed and demonstrated. These methods often combine a physical template with some external influence, such as capillary forces [68, 69], electrostatic forces [70, 71], covalent bond formation [72], slow sedimentation of particles from solution [73], magnetic levitation [74], etc. In Chapter two we use light as an external force to assemble a square array of particles, using a square lattice photonic crystal as a template. The square is but one example of a non-hexagonal structure – in principle this technique should allow for assembly of arbitrary geometries. In thesis I will describe a technique, called light-assisted templated self-assembly (LATS), for assembling particles into non-fcc lattices using photonic crystal slabs as templates. We believe that LATS

will enable the assembly of novel, bottom-up devices prohibited by existing self-assembly techniques.

1.7 – Fabrication

The photonic crystal devices used in experiments in this thesis were fabricated in USC's clean room. The process is shown diagrammatically in Fig. 2. It begins with a double-side polished silicon-on-insulator wafer with the following layers: 250 nm Si device layer, 3 μm buried oxide layer, 600 μm silicon handle layer. After solvent and O_2 plasma cleaning, plus a dip in hydrogen fluoride to remove the native oxide, electron beam resist is spincoated onto the wafer at 3,000 rpm for 60 seconds, resulting in a layer approximately 300 nm thick. The resist is Poly(methyl methacrylate), i.e. PMMA, with a 4% concentration in anisole and a molecular weight of 950K. The sample is baked at 170 $^\circ\text{C}$ for 70 minutes to evaporate the solvent. The samples are then exposed in the Raith e-Line 150 system using an acceleration voltage of 30 kV and an aperture of 10 μm , which produces a current of approximately 40 pA. The exposure pattern is created in the Raith software using proximity-corrected doses and curved-features exposure mode.

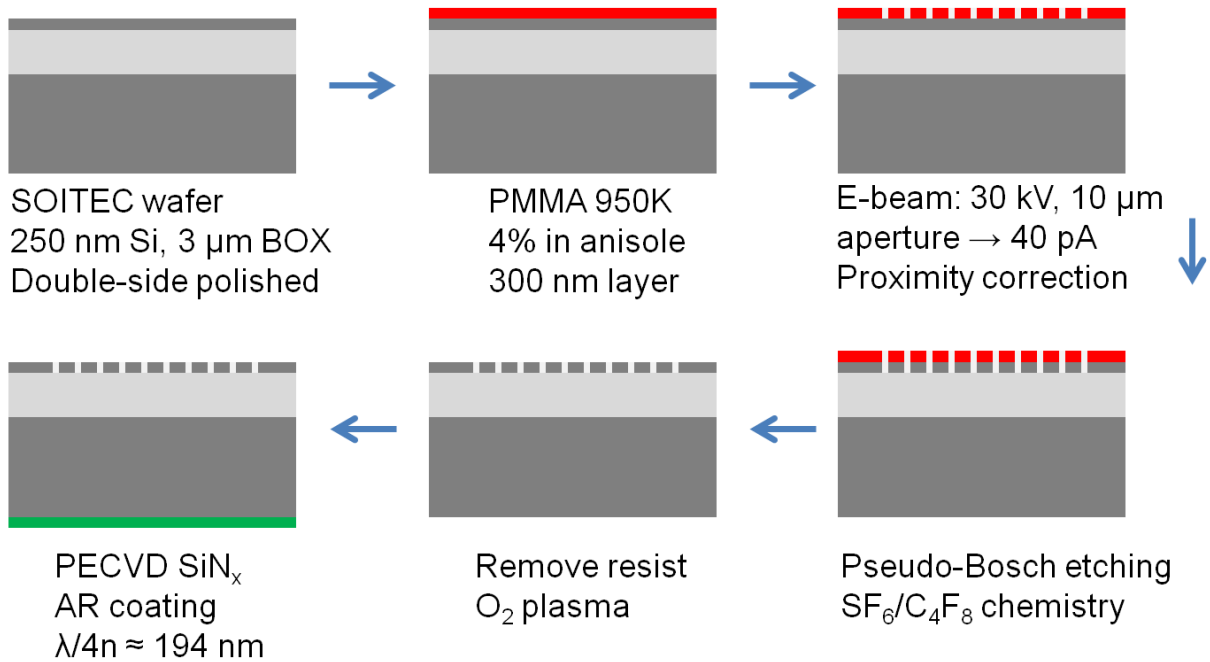


Figure 2. Schematic view of fabrication recipe. The process follows the order indicated by the arrows.

The samples are then developed in a 1:3 mixture of methyl isobutyl ketone (MIBK) to isopropyl alcohol (IPA) for 45 seconds, followed by a rinse in IPA for 45 seconds. Etching is done in the Oxford DRIE system using a modified Bosch process with the following parameters: 33.0 sccm of SF₆ (etchant), 57.0 sccm of C₄F₈ (polymer coating for protecting sidewalls), 20 mT chamber pressure, 30 W inductively-coupled plasma (ICP) power, 600 W reactive ion etching (RIE) power, 49 seconds etching time. The modified Bosch etching recipe was developed following Henry *et al.* [75], and produces smooth, vertical sidewalls (see Figure 3a). After stripping the resist and cleaning the sample, an anti-reflection layer of 194 nm SiN_x is deposited onto the back surface of the sample using plasma-enhanced chemical vapor deposition (PECVD). See Figure 3b for a micrograph of a square lattice fabricated using this recipe.

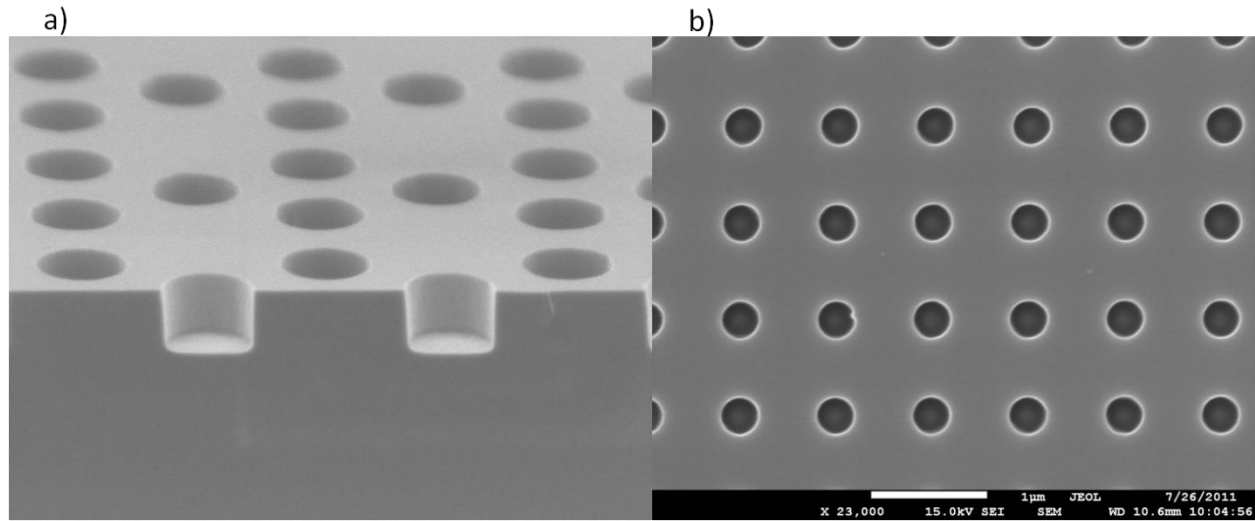


Figure 3. Samples fabricated using pseudo-Bosch etching recipe developed for use in the USC clean room. (a) Side view of Suzuki lattice etched into plain Si wafer and then cleaved along the patterned area. The bottoms of the holes are flat, and the sidewalls show smooth, vertical features. (b) Top view of square lattice sample showing excellent uniformity.

Microfluidic chambers are used to deliver polystyrene particles to the photonic crystals. The chambers are fabricated on a round glass coverslip 2 mm thick and 1 inch in diameter. After cleaning, the glass is spincoated with AZ 4620 positive photoresist for 60 seconds at 3,000 rpm, resulting in a thickness of approximately 8 μm . The sample is baked on a hotplate at 100 $^{\circ}\text{C}$ for 10 minutes to evaporate the solvents, then exposed in the MJB3 aligner with a dose of 300 $\mu\text{J}/\text{cm}^2$. The exposed resist is then developed using AZ400K for 5 to 6 minutes, resulting in a square of photoresist in the center of the glass with 8 mm sides (this is the inverse of the microfluidic chamber). A mixture of polydimethylsiloxane (PDMS) and a curing agent is prepared and a conformal layer is spincoated on top of the glass with the square of photoresist at 5,000 rpm for 60 seconds. The final thickness of the PDMS is at the edges of the glass side is approximately 5 μm . Thinner layers of PDMS can be prepared by diluting the mixture with tert-Butyl alcohol [76]. This sample is then cured in a 65 $^{\circ}\text{C}$ oven for 2 hours, thereby solidifying the

PDMS (see Figure 4). The final step is to cut away the square area above the photoresist using a razor blade and then to dissolve the photoresist with acetone. This results in a 5 μm high microfluidic chamber in which the walls are made of PDMS, the ceiling is glass, and the floor is the SOI sample.

To prepare the sample for the assembly experiment, which is described in greater detail in Chapter two, the SOI piece is bonded to an unpatterned glass coverslip with a 1 inch diameter using AZ 4620 photoresist. This coverslip is then placed in a threaded rotary stage with an inner diameter of 1 inch. A few drops of the particle solution are spread over the surface of the sample, and then the glass coverslip with the PDMS chamber is pressed down onto the sample. A threaded metal ring is screwed into place in the rotary stage, thereby sealing the chamber. See Figure 4 for a photograph of the prepared sample.

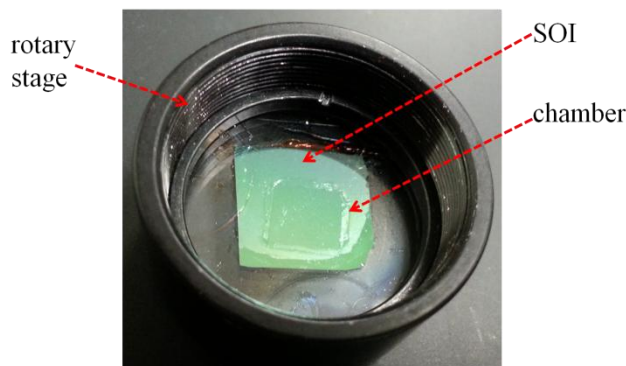


Figure 4. Sample mounted on 1-inch glass slides, immersed in particle solution, and sealed with PDMS chamber on glass.

1.8 – Experimental Set-up

A schematic of the experimental set-up is shown in Figure 5. The laser is a Santec TSL-510 with a tuning range from 1500 nm to 1620 nm, and a maximum output power of 28 mW, and is operated in continuous wave mode. The EDFA has a fixed output of 320 mW from 1535 nm to

1565 nm, and a linewidth of approximately 1 nm. There is an adjustable neutral density filter for controlling the power. The ND filter is connected to a single-mode fiber, which couples the light to free space with a fiber-to-free-space collimator. A polarizer and a half-wave plate allows for control over the polarization state of the beam. A beam splitter and a germanium photodetector are used to monitor the power in the beam. A long working distance microscope objective is used to focus the beam from the back of the sample onto the front sample surface. A variety of objectives and lenses are available: 5X with NA = 0.12, 10X with NA = 0.26, 20X with NA = 0.40, and 50X with NA = 0.42. For certain experiments we used achromatic doublet lenses instead of objectives – the range of NA values was similar.

The diameter d of a Gaussian beam at its focus can be determined by the formula

$$d = \frac{2\lambda}{\pi \cdot NA}$$

where λ is the free space wavelength of the beam and NA is the numerical aperture of the optic component (lens, objective) used to achieve the focus. These values were corroborated using the knife-edge method. Briefly, a metallic surface was mounted at the position of the sample and moved in controlled increments of 5 μm across the beam. The values of power recorded at the photodetector represents the integral of the beam power with respect to position. Taking the derivative of the measured values allowed us to recapture the Gaussian power profile. The diameter is then taken as the $1/e^2$ value of this Gaussian.

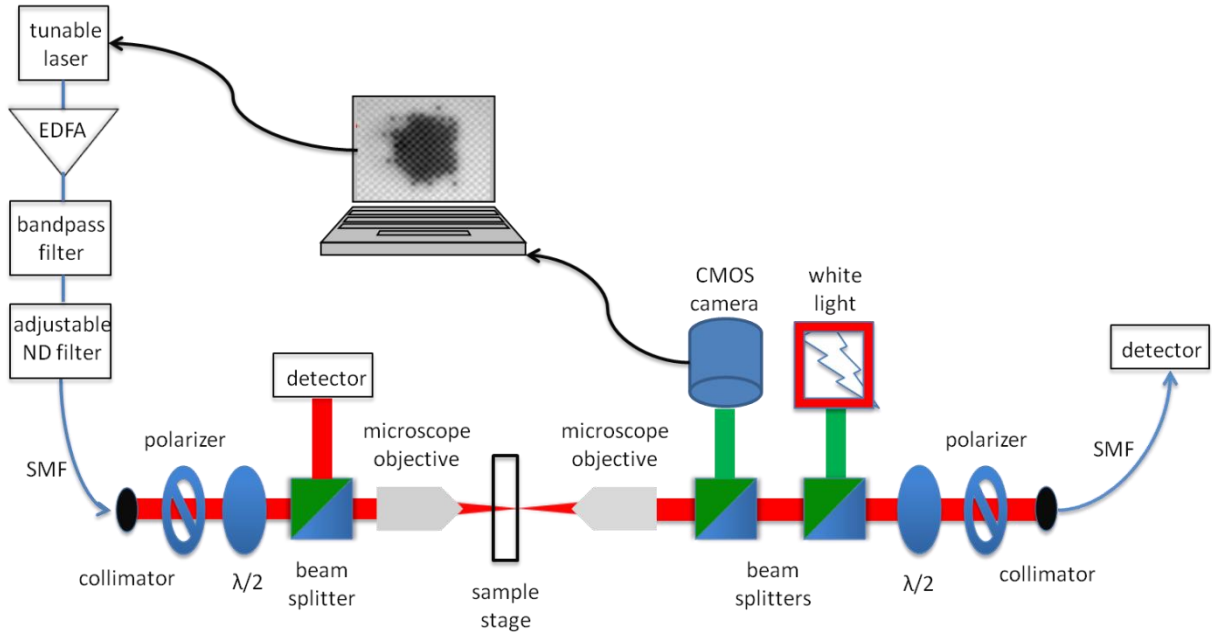


Figure 5. Schematic of experimental set-up used to characterize samples and perform assembly experiments.

On the other side of the sample there is a second microscope objective for collecting the transmitted light. In addition, this objective is used to image the particle movement using a CMOS camera and a white light source. A second set of polarization control optics is used to enable crossed-polarization measurements, which simplify the alignment of the set-up and improve the characterization of the sample. A second collimator is used to couple the light back to a single-mode fiber, which is connected to another germanium detector. The operation of the laser and detector is controlled by a computer running LabVIEW, which is also used to monitor and record the camera output. The set-up as described has the excitation at the back of the sample and the collection at the front of the sample, but by swapping the fibers between the laser and the detector, it is possible to reverse this order.

Chapter 2 – Light-Assisted, Templated Self-Assembly of Dielectric Particles

A version of this Chapter was published as reference [77].

2.1 – Introduction

In this Chapter I describe the first experimental demonstration of LATS, assembling a square array of over 100 polystyrene particles near a silicon photonic crystal slab. This method, ideally suited for on-chip integration, should provide a platform for flow-through, serial fabrication of 2D- or 3D-nanostructured materials, all-optically tunable photonic devices, and lab-on-a-chip applications.

The LATS process is shown schematically in Figure 6. Light is incident from below on a photonic crystal slab, which consists of a silicon device layer patterned with a periodic array of air holes. The slab is designed to support guided-resonance modes, electromagnetic modes for which the light intensity near the slab is strongly enhanced [78]. Previous work has theoretically predicted [79] that when the incident laser is tuned to the wavelength of a guided resonance mode, nanoparticles will be attracted toward the slab. The attractive, optical force arises from a strong electric field gradient just above the slab surface. In addition, the nanoparticles will experience lateral optical forces due to the electromagnetic field structure of the guided resonance mode, resulting in the assembly of a nanoparticle array.

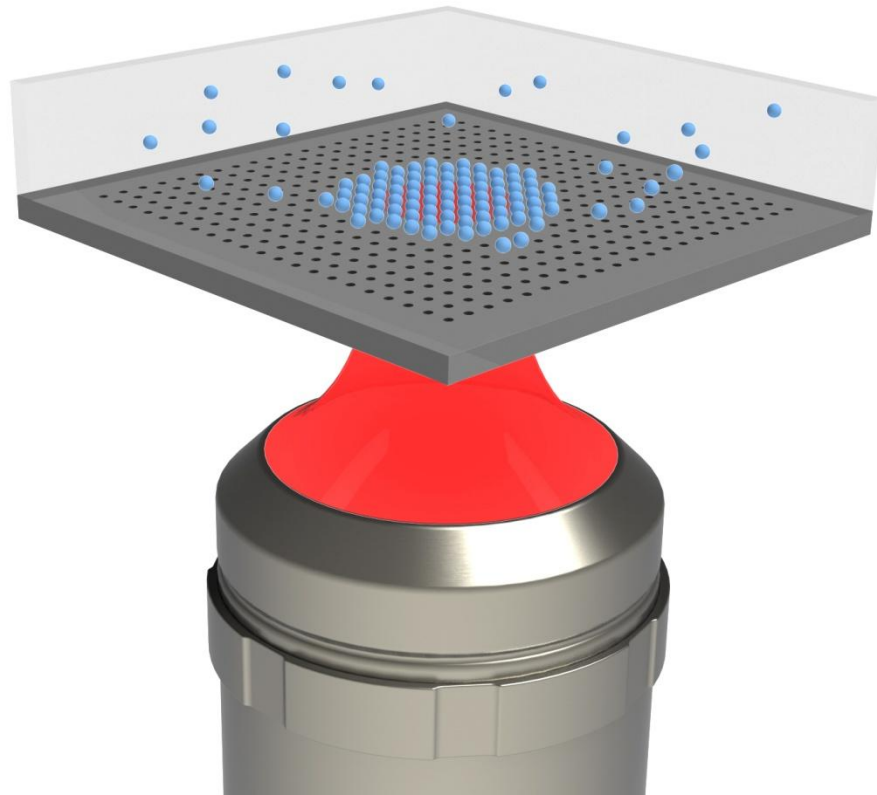


Figure 6. Schematic of light-assisted, templated self assembly (LATS). Incident light from below excites a guided resonance mode of a photonic crystal slab, giving rise to optical forces on nanoparticles in solution. Under the influence of the forces, the nanoparticles self assemble into regular, crystalline patterns.

Unlike traditional colloidal self assembly, for which free energy minimization results in hexagonal, close-packed structures, our process is not subject to such constraints. In this Chapter, we experimentally demonstrate the formation of a square lattice as one such example. Indeed, the use of light to drive the system dramatically alters the underlying potential landscape, potentially allowing for the formation of a range of complex lattices [79, 80] and multiparticle clusters [81]. Nanoparticle arrays assembled using LATS can be viewed as “programmable optical matter” [50]: turning the laser on and off will reversibly assemble or disassemble the

structure. Moreover, exciting different resonance modes of the photonic crystal, by adjusting the wavelength of the input laser, should allow different crystalline structures to be formed [79].

Light-driven assembly of multiparticle patterns has previously been achieved using structured light fields generated by interference fringes, holography, spatial light modulators, or other methods [44, 46, 82]. Our approach differs crucially from previous work in that it exploits near-field, rather than far-field, effects. Rather than generating a structured light beam via free-space optics, we use a simple, Gaussian input beam. The structured light field responsible for trapping is generated by the interaction of light with the photonic crystal device. Here, we demonstrate the method using an external laser incident on a photonic crystal slab. Ultimately, however, LATS could be carried out using a photonic crystal laser, allowing the integration of the light source with the trapping device and making our approach highly suitable for on-chip integration. We thus expect a wide range of applications from all-optically tunable photonic devices, to materials assembly, to biological trapping and manipulation.

2.2 – Device Design

We designed, fabricated, and characterized a photonic crystal slab for use in the LATS process. An electron micrograph is shown in Figure 7a. The device was fabricated in silicon using electron beam lithography and reactive ion etching (see Methods). The dimension and spacing of the holes was designed to support doubly-degenerate guided resonance modes near $1.55 \mu\text{m}$. The lattice constant a is 860 nm , and the hole radius is $0.174a$ (150 nm). The thickness of the silicon device layer is 250 nm . The magnetic field profile resulting from an x -polarized, incident plane wave is shown in Figure 7b. Fields were calculated using the three-dimensional finite-difference time-domain method (FDTD). The field-profile for a y -polarized incident wave is

rotated by 90 degrees. Figure 7c shows the measured transmission spectrum of the device.

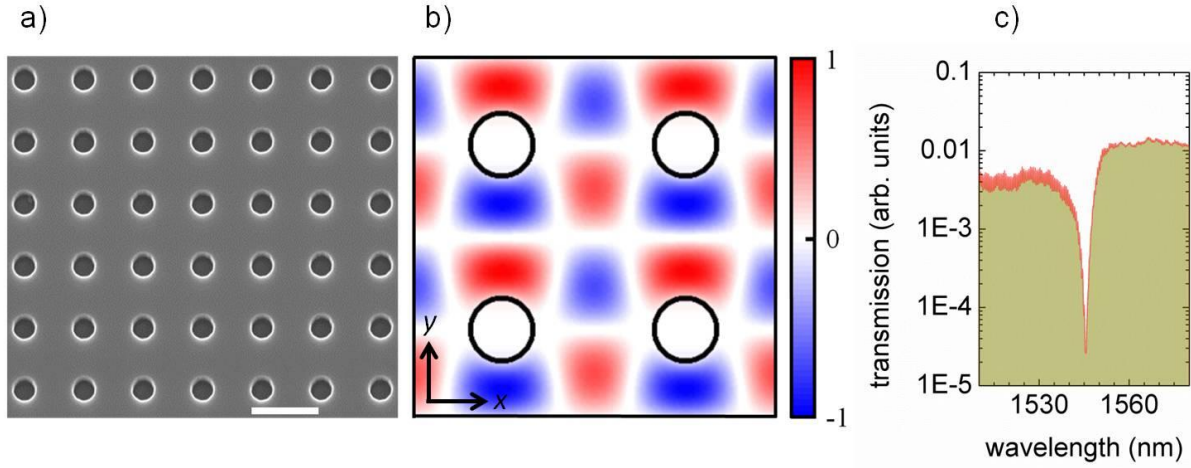


Figure 7. Square lattice photonic crystal. (a) SEM image of photonic crystal slab. The scale bar in the inset is 1 μm . (b) 3D FDTD simulation of the magnetic field (H_z) for a normally-incident, x -polarized plane wave. Circles represent the positions of holes; four unit cells are shown. (c) Measured transmission spectrum (log scale).

The guided resonance mode appears as a dip in the spectrum. The quality factor Q was determined to be ~ 170 by fitting to a Fano-resonance shape.

2.3 – Results

We carried out the assembly process in a microfluidic chamber filled with 520 nm diameter polystyrene particles, using a laser power of 64 mW. Figure 8 shows snapshots of the LATS process. The photonic crystal lattice is visible in the background of each frame. When the laser beam is turned on, nanoparticles are attracted to the slab, and begin to occupy sites of the square lattice (Figure 8a). As time progresses, additional particles diffuse into the region where the beam intensity is high, and begin to form a cluster (Figure 8b). Eventually, a regular array of particles is formed (Figure 8c). The square symmetry of the assembled particles is evident from the picture. When the laser beam is turned off, the particles immediately begin to disperse and

diffuse away from the slab (Figure 8d). Full videos of the assembly and release processes are included in the Supplementary Information. The frames in Figure 8 were recorded with a

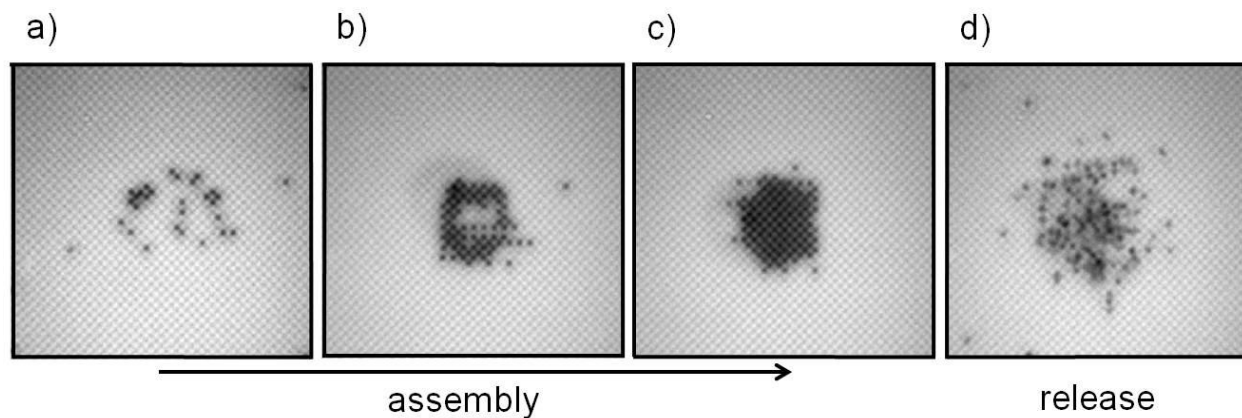


Figure 8. Light-assisted, templated self assembly of 520 nm diameter particles above a photonic crystal slab. The square lattice of the slab is visible in the background, oriented at 45° with respect to the camera. (a-c) Sequential snapshots taken with the light beam on. (d) Snapshot taken after the beam is turned off.

dilute particle solution for clarity of imaging, and represent an elapsed time of approximately one hour. Faster cluster formation occurs with solutions of higher concentration.

We have explored the dependence upon power, wavelength and particle diameter. The size of the cluster, i.e. the number of particles trapped, decreased in a monotonic fashion as the power was decreased, or as the wavelength was tuned away from resonance. We also attempted to assemble two other sizes of polystyrene particles, 380 nm and 1 μm . We were able to assemble a square lattice of 380 nm particles. The trapped particles exhibited more Brownian motion when compared to the 520 nm particles. We did not observe trapping with 1 μm particles. This is likely due to the increased scattering cross-section, which results in a net repulsive force away from the slab.

Each site of the square lattice may be viewed as an optical trap. We used particle-tracking software to analyze particle motion for fully-assembled clusters (see Methods). Figure 9a shows the recorded particle positions extracted from a 20 second video. The incident light was polarized along the x -direction of the lattice. The figure shows that the particles tend to stay above the holes in the photonic crystal, with some variation in position over time. Each blue ellipse represents a fit to the data in a single unit cell. It can be seen that the variation in particle position increases at the edge of the trapping region, due to the reduction in power away from the center of the beam.

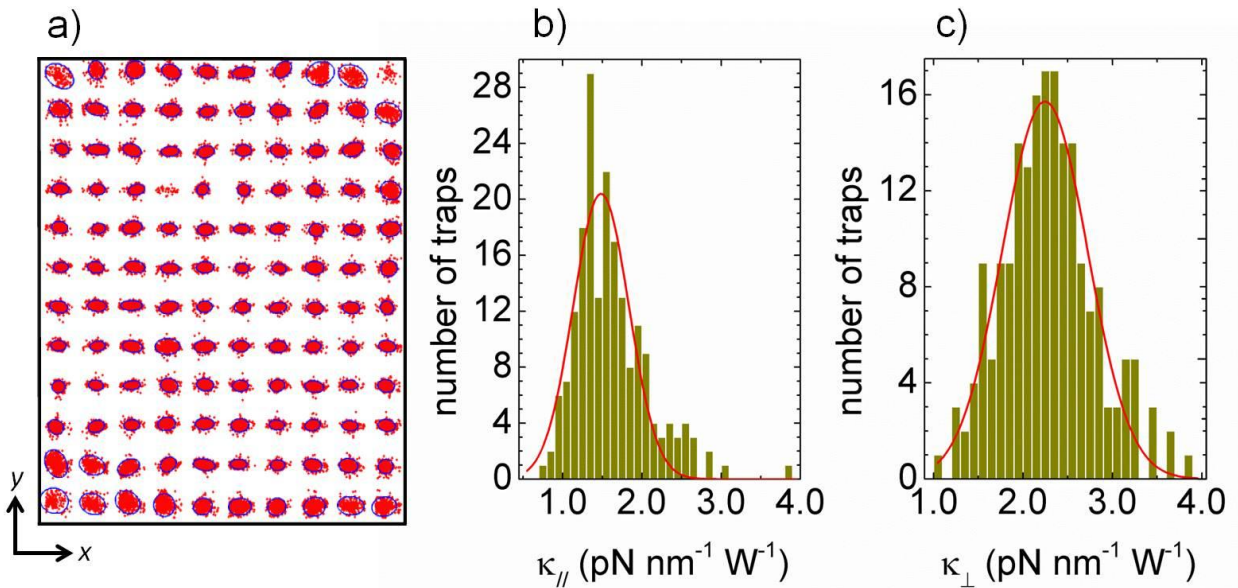


Figure 9. Trap stiffness for incident, x -polarized light. (a) Particle positions (red dots) extracted from a 20 second video. Blue ellipses represent two standard deviations in position. (b) Histogram of stiffness values in the direction parallel to the polarization of the incident light. (c) Stiffness in the direction perpendicular to the incident polarization.

The stiffness of each trap can be determined from the variance in particle position, as described in Section 1.3 [59]. Figures 9b and 9c show histograms of the in-plane stiffness values extracted from the videos. The stiffness of each trap was normalized to the local intensity in that unit cell

(see Methods). We observe that the power-normalized stiffness over the array of traps is normally distributed, both for the parallel and perpendicular stiffness. The mean parallel stiffness is lower than the perpendicular stiffness, as shown in Table 1 (0 ° angle).

We observe that the trap stiffness can be tuned by rotating the polarization direction of the incident light. When the incident light is polarized at 45° with respect to the lattice directions, the stiffness values are approximately the same in the x - and y -directions (Table 1). This is to be expected, since the incident light excites both of the doubly-degenerate modes with equal strength. At 90°, the stiffness in the parallel direction (y) is again lower than in the perpendicular (x) direction. The ability to tune the stiffness with incident light indicates the strong optical nature of our traps. The mean values of stiffness are comparable to those reported elsewhere in the literature for single particle traps [31].

Table 1. Polarization dependence of trap stiffness

angle (°)	κ_x (pN nm ⁻¹ W ⁻¹)	σ_x (pN nm ⁻¹ W ⁻¹)	κ_y (pN nm ⁻¹ W ⁻¹)	σ_y (pN nm ⁻¹ W ⁻¹)
0	1.48	0.35	2.25	0.48
45	1.88	0.52	1.79	0.46
90	2.08	0.40	1.39	0.29

Using the Stokes drag method (see Methods), we experimentally estimated the maximum force exerted on the particles by the traps to be 0.3 pN.

2.4 – Simulations

To understand how the optical forces result in the observed nanoparticle patterns, we calculated the force numerically (see Methods). Figure 10 shows the force on a 520 nm diameter particle whose bottom edge is 25 nm above the surface of the photonic crystal slab for x -polarized light. The background color represents the vertical force, where a negative force indicates attraction toward the slab. The force is negative, i.e. attractive, throughout the unit cell,

with the strongest vertical force occurring at the center of the holes. The arrows represent the in-plane forces, and are largely directed toward the center of the hole as well.

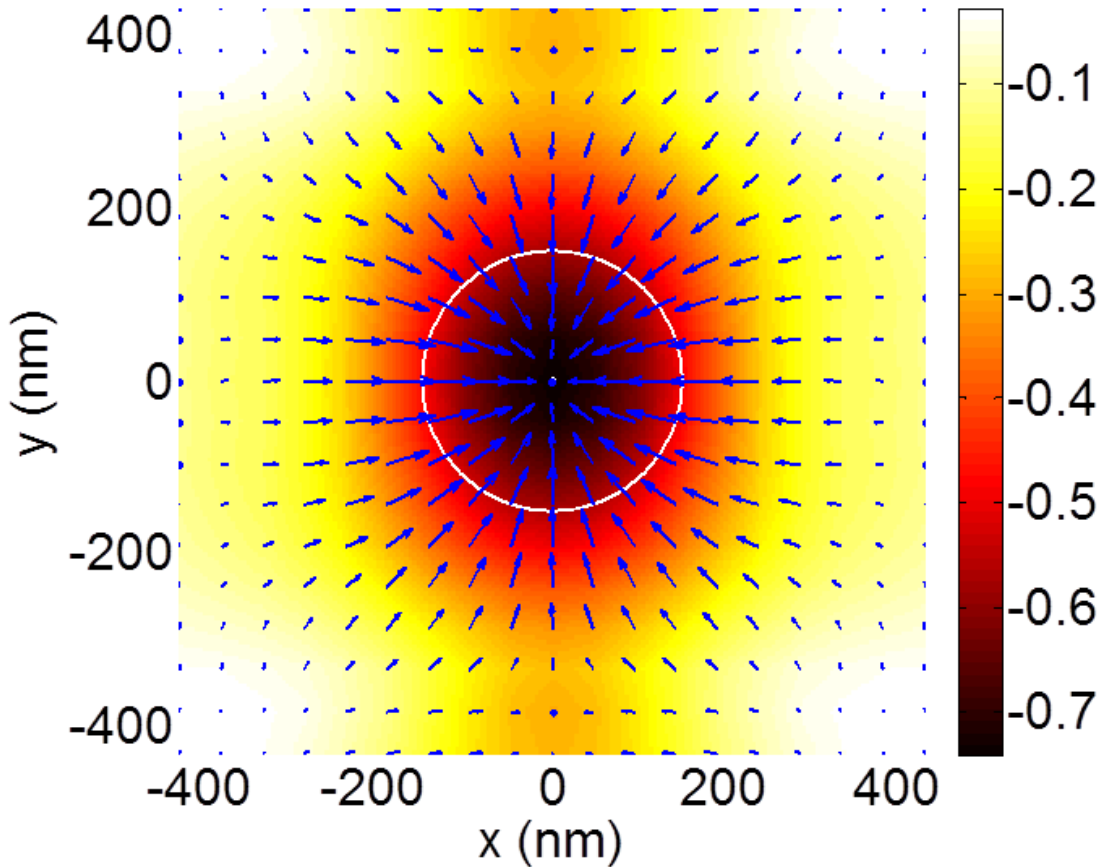


Figure 10. Calculated optical forces using the Maxwell stress tensor method. Force map in one unit cell. The white circle represents the position of a hole in the square lattice, and the color bar represents the vertical optical force in dimensionless units of Fc/P , where c is the speed of light, and P is the incident optical power. A negative force indicates attraction toward the slab. The arrows represent the magnitude of the lateral optical force. For comparison with the vertical force, the maximum in-plane force has a value of 0.56.

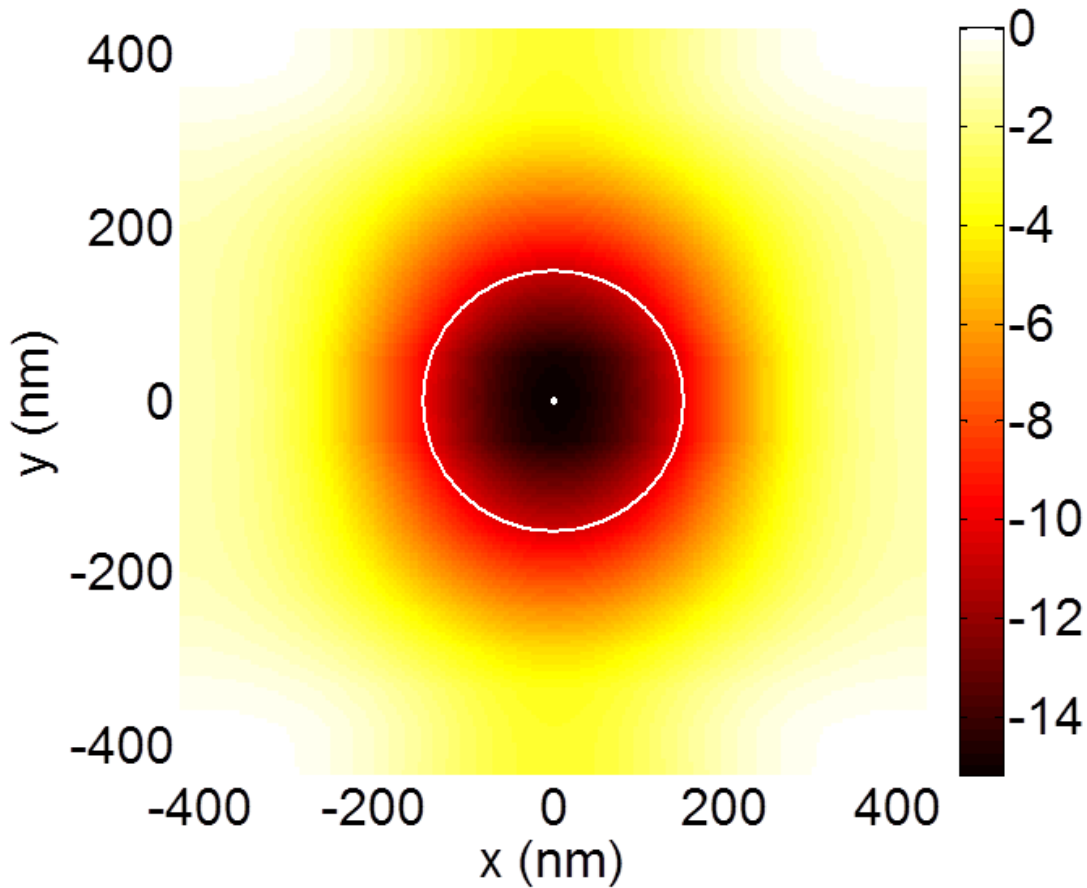


Figure 11. In-plane optical potential map in one unit cell. The map was obtained by integrating the in-plane forces shown in Figure 10. The colorbar shows the potential in arbitrary units. The maximum value within the unit cell was set to 0.

To determine the equilibrium position of the trapped particle, we calculate the optical potential due to the in-plane forces. As a reminder, all calculations are done with the particle at a fixed height of 25 nm from the surface. As can be seen in Figure 11, the deepest potential is clearly in the center of the hole, which corroborates the observed results from the experiments.

We determined that the threshold intensity for trapping was 134 μW per unit cell (see Methods). For this intensity, the calculated potential depth is 4.5 $k_B T$.

2.5 – Discussion

In summary, we have experimentally demonstrated the technique of light-assisted, templated self-assembly (LATS). Our technique uses the resonantly enhanced near field of a photonic crystal slab to create periodically spaced optical traps. Nanoparticles in solution are attracted to the slab and form ordered arrays. We have observed the assembly of 100 polystyrene particles with 520 nm diameter in a square lattice using 64 mW of incident power. We have measured the trapping stiffness as a function of incident polarization, and we have shown that the equilibrium trapping positions can be predicted via calculation of the optical forces.

Our technique can be extended to assemble larger numbers of particles by designing the photonic crystal slab to reduce the input power per area required for trapping. The input beam can then be spread over a larger area, resulting in a larger cluster. One approach to reducing the required power per area is to use a mode with a higher quality factor, resulting in higher near-field intensity. Another approach is to use slot-confinement effects to strongly localize the field in the trapping regions, as has been studied theoretically [80].

The LATS approach can be used to assemble complex structures with symmetries not constrained by the typical free energetic constraints; here we have demonstrated just one. We envision that judicious template design will allow for the assembly of a variety of lattice types with complex unit cells. Moreover, changing the wavelength of the incident beam to excite a different resonance can be used to reconfigure the particle arrangement [79]. The use of metal nanoparticles or quantum dots is also an area for future exploration. While in the current experiment with polystyrene particles we did not observe evidence of optical binding [83] or self-induced back-action [84], such effects may yield rich assembly behavior in alternate particle systems. I will talk about this further in Chapter three.

We anticipate that our technique will find applications in the fabrication of metamaterials and other photonic devices. For example, post-assembly polymerization could be used to transfer 2D nanoparticle arrays to another substrate. Our preliminary results indicate that it is also possible to assemble 3D arrays *in situ*.

LATS should also allow a variety of dynamic, real-time applications. One example is the use of the assembled, reconfigurable “photonic matter” as an all-optically tunable transmission filter. Other applications, based on particle dynamics in the 2D optical potential, include particle sorting [85, 86] and ratchet behavior [87]. We also expect that LATS may be extended for batch processing of biological objects, providing a novel tool for reconfigurable control over spatially-mediated biological interactions.

Finally, LATS naturally lends itself to compact integration on-chip. By fabricating the photonic crystal device in an active material, the light source could be integrated with the trapping device, allowing for system miniaturization.

2.6 – Methods

Details of the fabrication and experimental set-up were provided in Chapter one.

Stiffness analysis. After the assembly of a cluster, we recorded videos with a fixed exposure time of 33 ms, the fastest value available in our experimental set-up. Typical videos were 600 or more frames in length. Particle motion was analyzed using MATLAB algorithms written by Blair and Dufresne (<http://physics.georgetown.edu/matlab/>), which are modified versions of IDL routines written by Crocker and Grier.

The blue ellipses in Figure 9a are obtained by fitting the data in each unit cell. The direction and relative lengths of the major and minor axis are determined from the eigenvectors and eigenvalues of the scaled covariance matrix. The ellipse is drawn to represent a 95% confidence

interval: positions outside the ellipse will be observed only 5% of the time by chance if the underlying distribution is Gaussian.

The measured variances were corrected for motion blur due to the finite integration time of the camera and for the measured value of the diffusion coefficient (see below) [88]. We observed that the variance as a function of position within the cluster had a 2D Gaussian distribution. This is to be expected due to the spatial variation in intensity in the incident beam. We confirmed via 3D-FDTD simulations of a finite-size structure with Gaussian beam excitation that the field intensity above the slab has a Gaussian envelope. The stiffness values shown in Figure 9 are normalized to the local power at each trapping site, as determined by fitting the experimentally-measured variances to a 2D spatial Gaussian.

In order to account for the surface hydrodynamics near the photonic crystal, we directly measured the diffusion coefficient. We first assembled a cluster, then blocked the beam and performed a linear regression fit to the subsequent diffusion as a function of time [89]. A value of $0.56 \mu\text{m}^2/\text{s}$ was obtained.

Force measurement. After assembling a cluster, we increased the flow speed until all particles were released. We observed the release of the last, trapped particle at a fluid velocity of $30 \mu\text{m}/\text{s}$ for a laser power of 64 mW. In the low Reynolds number regime, the particle velocity v is related to the external force by the equation $F = \frac{k_B T}{D} v$, where k_B is Boltzmann's constant, T is the temperature, and D is the measured value of the diffusion coefficient.

Force and potential calculation. For each particle position within the unit cell, we performed an FDTD simulation to calculate the electromagnetic fields and obtained the optical force from an integral of the Maxwell Stress Tensor over a box just large enough to include the particle. The z -dependence of the force inside the hole was obtained from an exponential fit to the field

intensity above the slab. The power threshold for stable trapping was determined experimentally from the size of the stable cluster (16 unit cells, or 13.8 μm , in diameter). The Gaussian distribution of energy in the mode, obtained from a fit of the variance measurements, had a FWHM of 15 μm . Given the input power of 64 mW we find a peak intensity of 240 μW per unit cell, and a trapping threshold intensity at the edge of the cluster of 134 μW per unit cell.

Chapter 3 – Light-Assisted, Templated Self-Assembly of Metallic Particles

A version of this Chapter was published as reference [90].

3.1 – Introduction

It is natural to ask whether the LATS technique can be extended to form more complex structures, such as metallic or mixed metallo-dielectric [81] systems. Such structures are of great interest for applications such as plasmonics and metamaterials [91-95], and can potentially be extended to enable multiplexed, on-chip biological trapping and analysis [28, 96-98]. For metallic particles, however, it is unknown whether and how the types of interparticle interactions observed in template-free systems [54-56, 99-101] change the nature of the LATS process.

In this Chapter, we observe dramatic effects of interparticle interactions in LATS experiments on gold nanoparticles, resulting in the assembly of completely different nanoparticle patterns. While the template provided by the photonic crystal slab is two-dimensionally periodic, the assembled gold particles form one-dimensionally periodic chains. The orientation of the chains, which may contain as many as 15 particles, can be rotated with the incident laser polarization. We observe that interparticle interactions result in a *self-stabilization effect*; particles in chains remain trapped for much longer than isolated particles. Our results suggest that the emergence of 1D periodic patterns within a 2D periodic optical potential can be understood in terms of a competition between particle-template and particle-particle interactions.

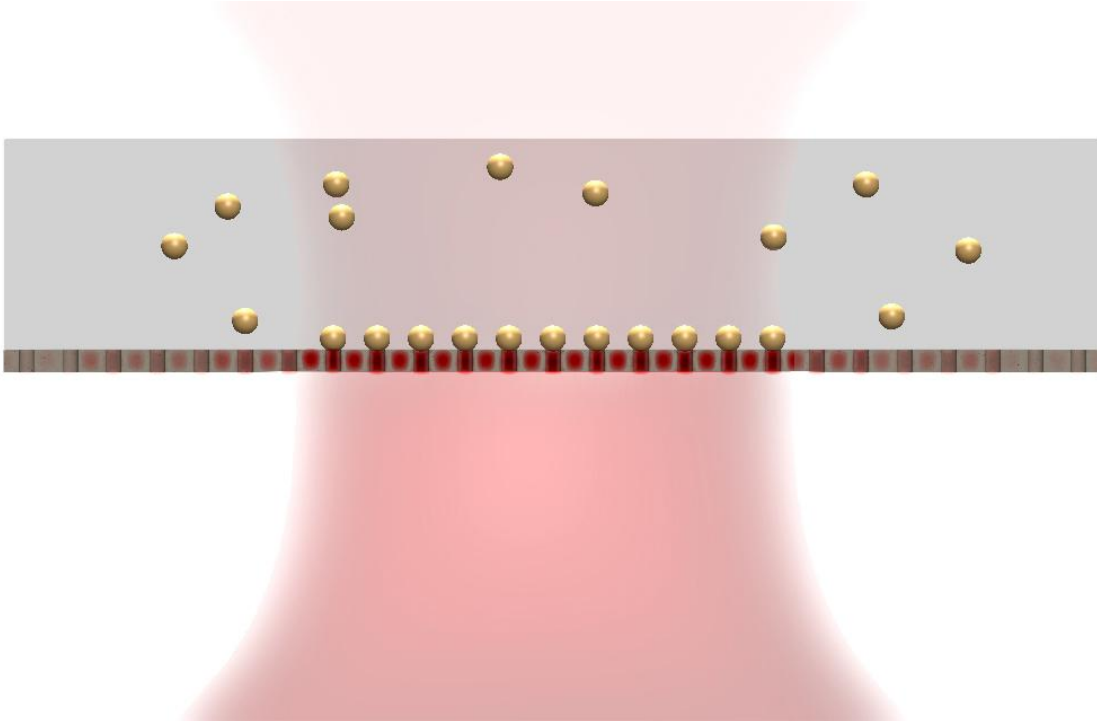


Figure 12. Schematic view of light-assisted, templated self assembly (LATS). Normally-incident light excites a mode in the slab whose evanescent decay attracts particles toward the slab.

The system is shown schematically in Figure 12. Light is incident from below on a photonic crystal slab, which consists of a silicon device layer patterned with a periodic array of holes. For a certain laser wavelengths, the incident light will excite a spatially extended mode in the slab called a guided resonance mode [102]. Such modes have strong electromagnetic field intensities that decay exponentially away from the upper surface of the slab. The gradient in the electric field intensity attracts particles in solution toward the slab, which serves as a template for assembly [77].

3.2 – Device Design

We designed, fabricated, and characterized a photonic crystal template for use in the current experiment. Figure 13a shows a scanning electron micrograph of the device, which contains a

square lattice of holes in a 250 nm thick silicon device layer. The lattice constant a is 780 nm, and the hole radii are $r = 0.106a = 82.5$ nm and $0.086a = 67$ nm. The lateral extent of patterned photonic crystal region was $50 \mu\text{m} \times 50 \mu\text{m}$. The device was designed to support a doubly-degenerate, TE-like mode near $1.55 \mu\text{m}$. The measured transmission spectrum of the device with x -polarized light is shown in Figure 13b. The dip in the transmission spectrum represents the excitation of the guided resonance mode. A quality factor Q of approximately 880 was obtained by fitting the spectrum to a Fano-resonance lineshape. Figure 13c shows the electric field intensity profile (E^2) for x -polarized incident light, which was calculated using a 3D finite-difference time domain (FDTD) simulation. The field profile for y -polarized incident light is rotated by 90° . Figure 13d shows the same simulation with light polarized at $+45^\circ$ with respect to the x -direction. The electric field intensity is largely concentrated in the holes in both cases.

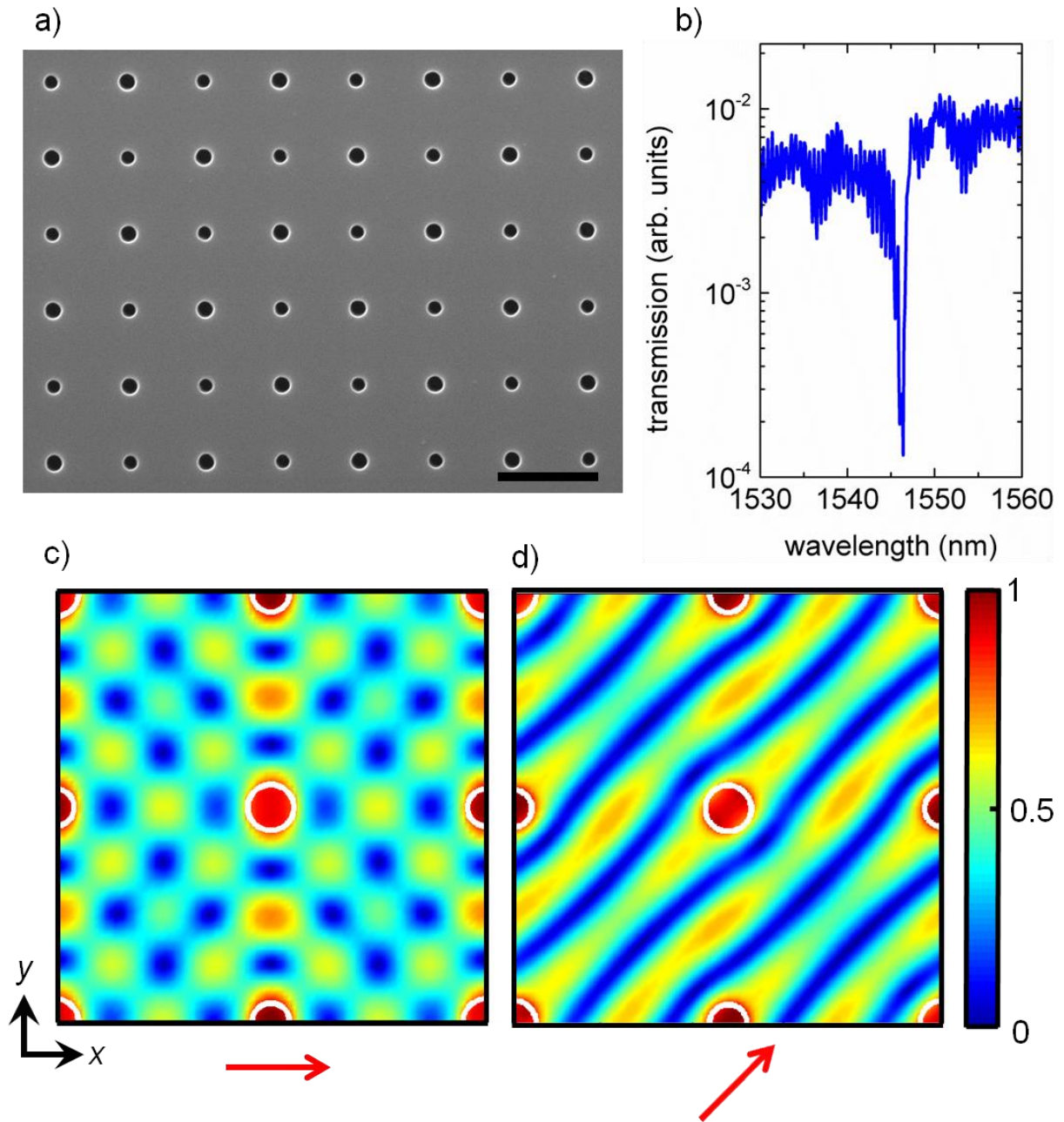


Figure 13. Silicon photonic crystal device. (a) Scanning electron micrograph of the device used in the experiments. The scale bar represents 1 μm . (b) Measured transmission spectrum of the device. (c) Mode profile (E^2) on resonance for x -polarized incident light calculated using 3D-FDTD. The circles represent the positions of the holes. (d) E^2 for light polarized at $+45^\circ$ with respect to the x -axis.

Assembly experiments were carried out in a microfluidic chamber filled with 200 nm diameter gold nanoparticles, using a laser power of 64 mW. The chamber was less than 1 μm high to minimize hydrodynamic effects [103]. (See Methods for details of the chamber fabrication.)

3.3 – Results

Figure 14 shows results from a typical experiment. Unlike our previous results for polystyrene particles, the trapped gold particles do not form close-packed arrays. Instead, we observe the formation of chains. In each panel of Figure 14, the incident light polarization is indicated by red arrows. In Figure 14a, the polarization is aligned with a diagonal of the square lattice. Two chains are clearly visible, which are oriented at 90° with respect to the incident polarization. When the polarization is aligned with the nearest-neighbor direction of the square lattice (Figure 14b), chains form along both diagonals. For a polarization aligned with the other diagonal of the square lattice (Figure 14c), chains are again observed perpendicular to the polarization. Upon blocking the beam, the particles immediately diffuse back into solution. Detuning of the trapping wavelength by ± 1 nm (comparable to the FWHM of the resonance) also results in release of trapped particles. The measured stiffness for trapped particles had an average value of $66 \text{ pN nm}^{-1} \text{ W}^{-1}$, which is more than an order of magnitude greater than previous experiments with polystyrene particles [77], as reported in Chapter two. The formation of 1D chains within the 2D-periodic near field of the photonic crystal slab indicates that interparticle interactions are playing a strong role in the observed behavior.

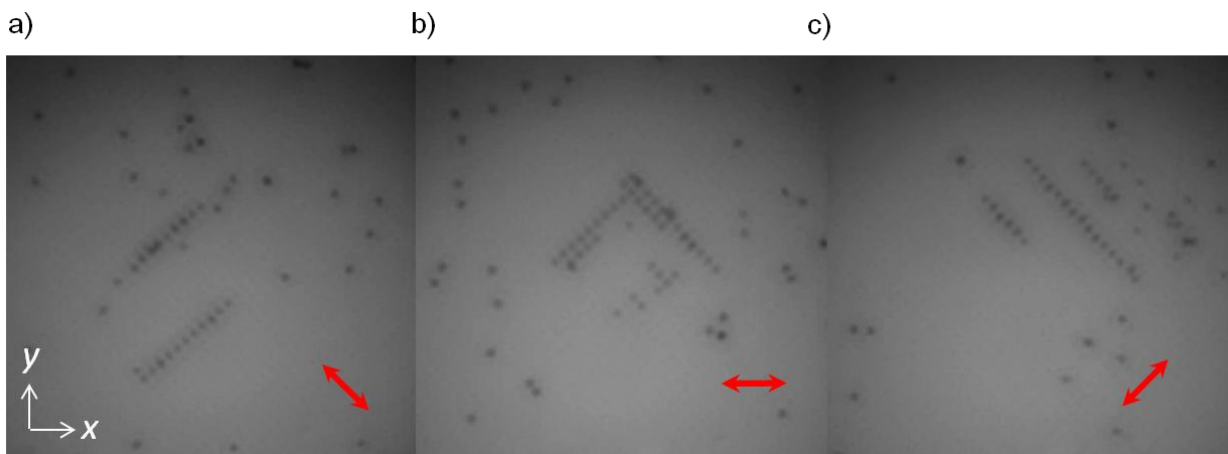


Figure 14. Assembly of nanoparticle chains. (a) The incident light is initially polarized at -45° with respect to the x -axis, as indicated by the red arrow. (b) The polarization is rotated to align with the x -axis. (c) The polarization is rotated to $+45^\circ$.

To quantify the process of chain formation and reconfiguration, we recorded video of an assembly experiment. We counted the number of trapped particles in each video frame that were in a chain of at least three particles. Untrapped particles, trapped particles that were isolated, and trapped particles that had just one nearest neighbor were not counted. These results are shown in Figure 15.

At the beginning of the experiment, the polarization is at -45° with respect to the x -direction, as shown in the first pane of the figure. The number of particles trapped in chains oriented at 90° with respect to the polarization increases quickly (grey line), whereas particles in chains that are aligned with the polarization are observed only occasionally (black line). The initial rate of chain formation is limited by delivery of particles to the trapping volume and can be decreased by using a solution with a higher particle concentration. The fluctuations in particle number are due to trapping and untrapping of particles with time.

The polarization is then rotated by 45° to align with the x -direction of the lattice. While the original chains largely persist, we observe chains forming along the opposite diagonal. Finally,

the polarization is rotated another 45° , and immediately we notice that the original chains disappear, whereas the newer chains persist. We can thus control the orientation of chains by changing the polarization of the incident light.

The relationship between incident light polarization and chain direction was repeatable across multiple experiments recorded on different days. These results are summarized in Table 1, which represents data taken from more than 14,000 frames. Since the videos were recorded in time-lapse fashion at one frame per second, the table represents almost four hours of data. At no time did we observe the formation of 2D clusters, despite the extended, 2D periodic nature of the resonant mode of the photonic crystal slab. In each experiment, the initial arrangement of trapped particles was seemingly random, but eventually the pattern collapsed into a 1D chain or chains.

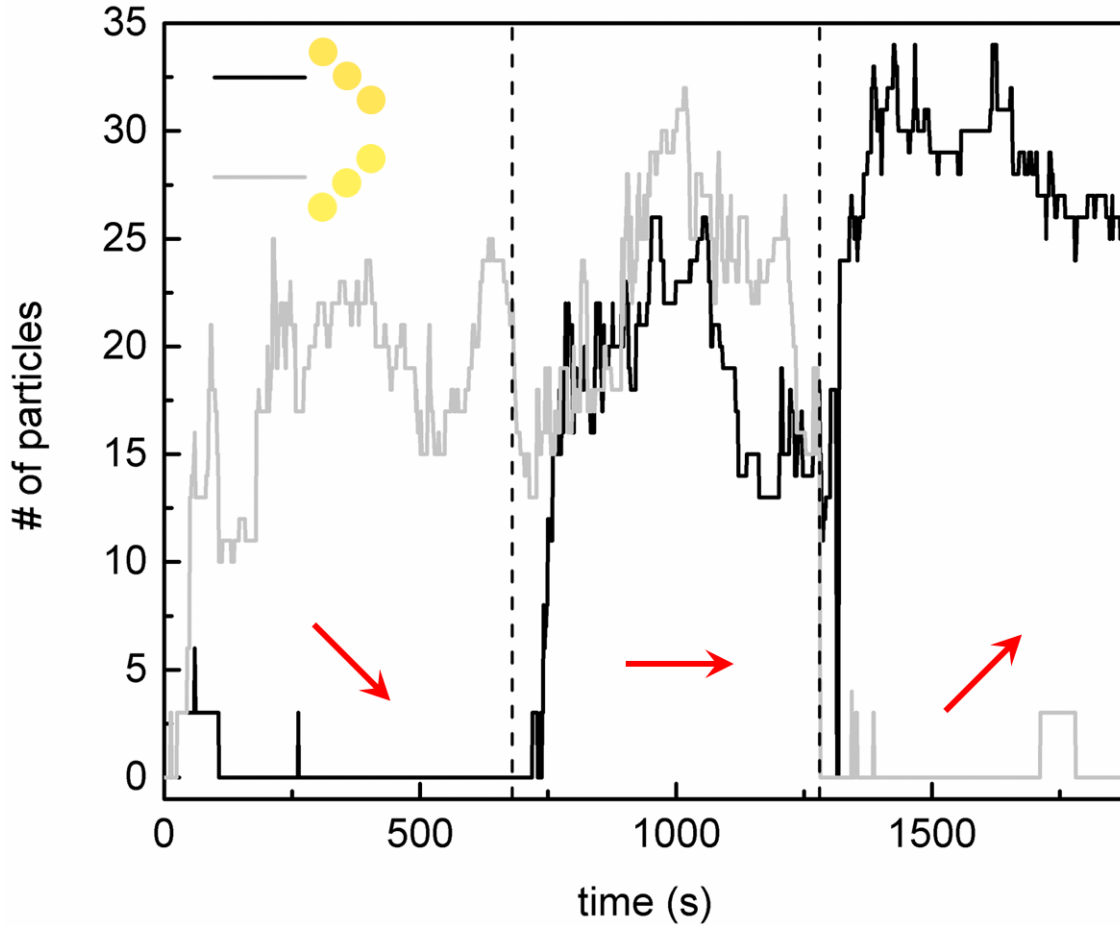


Figure 15. Chain formation as a function of polarization angle. The red arrows indicate the incident polarization, and the black and grey lines represent the number of particles in chains with orientations indicated in the legend. Vertical, dashed lines represent the time at which the polarization was changed.

We note that chain formation was observed in a variety of devices and experimental conditions. In addition to the square lattice with perturbed holes along alternating diagonals reported here, we also observed chain formation in a square lattice with the same lattice constant and uniform hole sizes. The behavior was also robust to total device size. We fabricated devices that were $100\ \mu\text{m} \times 100\ \mu\text{m}$, and devices that were written in a circular pattern with a $50\ \mu\text{m}$ diameter, each having the same lattice parameters. In all cases we observed similar behavior.

For the specific device reported above in Figure 14, trapping of particles in chains was observed for power levels between 30 mW and 200 mW.

Table 2. Average number of particles trapped in chains along different orientations as a function of incident polarization. The average is taken over approximately four hours of video.

Orientation of chains	Polarization		
	↖	↑ or →	↗
↖	1.14	17.35	20.74
↗	17.66	16.32	1.55

To probe the effects of interparticle interactions on trapping stability, we analyzed the length of time that particles remained trapped. Figure 16a shows the results for particles that were part of chains. Blue circles indicate trapping sites that were occupied by a particle in a chain at any point during the video, and the colorbar indicates the maximum length of time, in seconds, that the site remained occupied. The video was 2000 frames in total. Sites near the center of chains had the longest occupation times, reflecting the fact that chains tend to grow outward from the center. Figure 16b shows results for particles that were not part of chains. The maximum time that a site was continuously occupied by a particle not in a chain was 255 s, much shorter than the 1915 s value observed for particles in chains in Figure 16a. The average value over all trapping sites was also much shorter for particles not in chains than for particles in chains (12 s vs. 180 s, respectively). This trend held across several videos whenever the polarization was aligned with a diagonal of the lattice. We conclude that the chains of gold particles are *self-*

stabilizing: particles that join chains remain stably trapped for longer than isolated particles trapped elsewhere on the template.

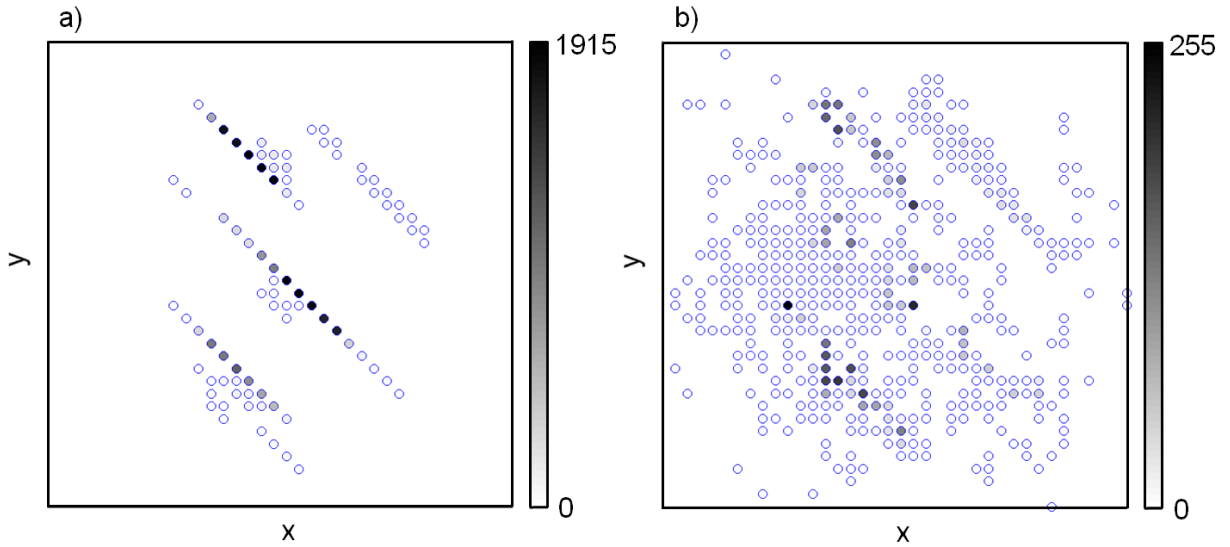


Figure 16. Stability of trapped particles. (a) Maximum length of time (in seconds) per trap site that particles in chains remain trapped. (b) Maximum length of time per trap site that particles not in chains remained trapped. Blue circles indicate trap sites that were occupied at any point during the video.

Our experimental results suggest that pattern formation (e.g. the emergence of particle chains) arises from the competition between particle-template and particle-particle interactions. A calculation of the optical forces acting on a single particle (see Figure 17) predicts that each hole in the template is a stable trapping site, and that the optical field pulls the metallic particle down into the hole. Absent any interparticle interactions, we would expect a regular, close-packed square lattice of particles to form. Interparticle interactions change this behavior. Given an initially trapped particle, a nearby particle in solution will experience optical forces not only due to the template, but also due to the scattered field of the first particle. This interparticle interaction (similar to “optical binding” [49, 53, 54, 56, 83, 104]) will influence which trapping

site the second particle is most likely to settle in. Full numerical calculations of multi-particle trapping dynamics are computationally prohibitive and beyond the scope of this Chapter. However, we can gain some insight from a simplified model, which calculates the interparticle interactions due to an incident plane wave in water. The model predicts that given an initially trapped particle, interparticle interactions favor the nearest-neighbor sites perpendicular to the polarization direction, in agreement with experiment.

3.4 – Simulations

To compute the forces shown in Figure 17, we used 3D-FDTD to simulate the fields in the experimental geometry with a gold sphere of radius 100 nm at various positions within the unit cell [79]. The lower edge of the particle was at a fixed height 40 nm above the slab. We then used the Maxwell stress tensor method to compute the forces on the sphere. Each position within the unit cell represents one FDTD simulation with the sphere located at that position. Further information about the method can be found in Chapter two.

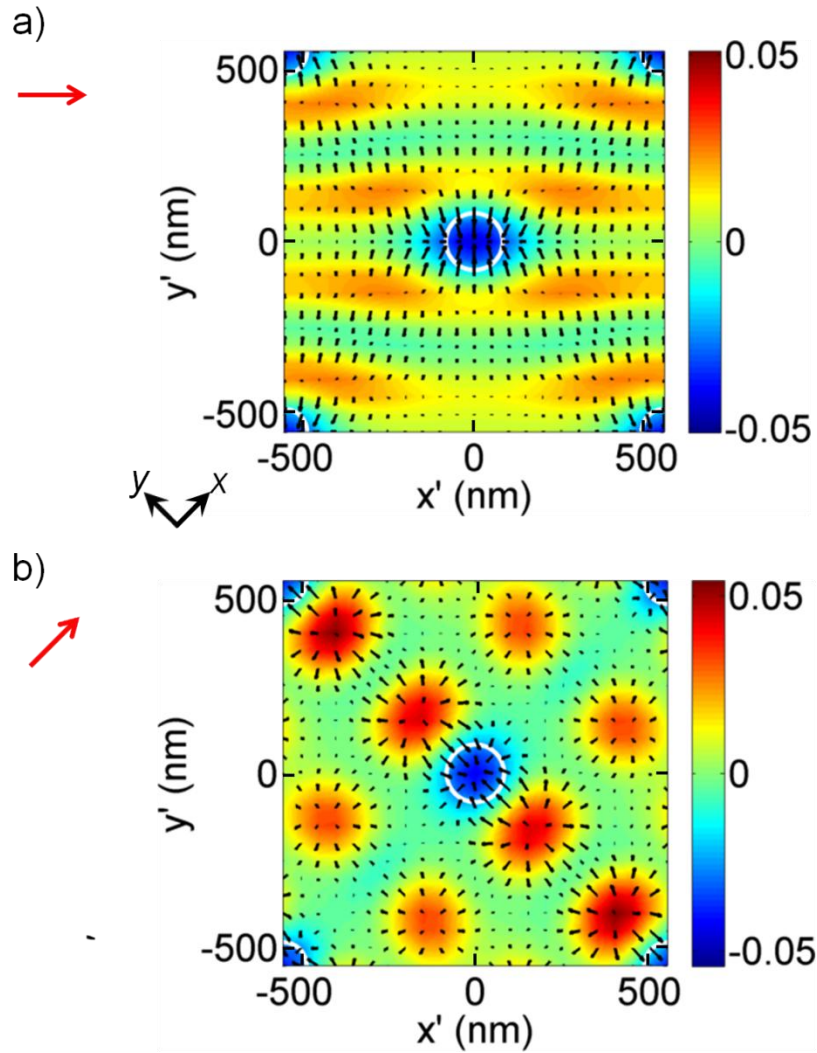


Figure 17. Forces calculated via the Maxwell stress tensor method in dimensionless units of Fc/P , where c is the speed of light in vacuum and P is the incident power. The background represents the vertical force, and the arrows represent the in-plane forces. Negative vertical force indicates attraction toward the slab. Note that the lattice is rotated by 45° with respect to the base square lattice. The length of the black arrow superimposed on each plot represents an in-plane force of 0.1. (a) Incident light is polarized along x' , i.e. along the diagonal of the square lattice. The maximum in-plane force has a magnitude of 0.035 in normalized units. (b) Incident light is polarized along the x -axis. The maximum in-plane force has a magnitude of 0.038.

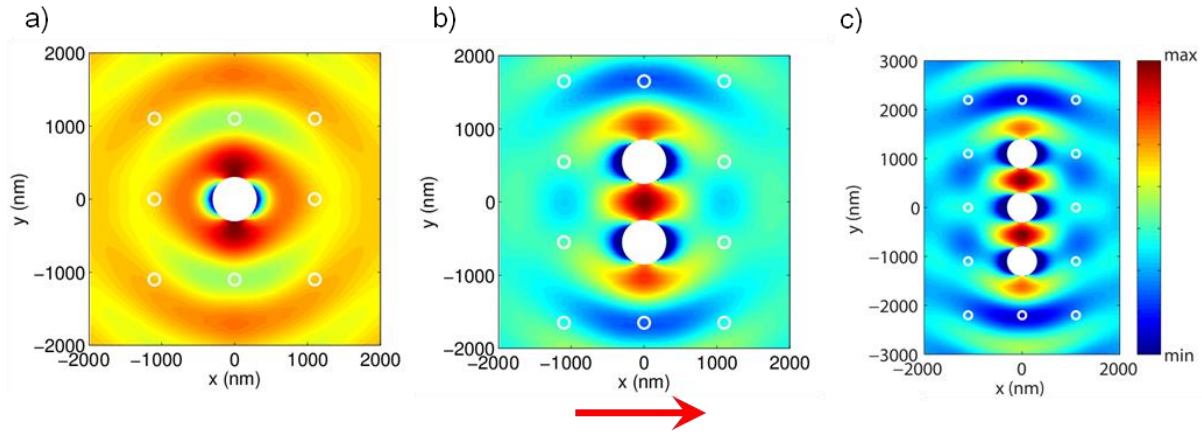


Figure 18. Potential energy surfaces for 200 nm diameter Au particles in water, illuminated by a plane wave with a vacuum wavelength of 1550 nm. The red arrow indicates the direction of polarization. (a) One trapped particle. (b) Two trapped particles. (c) Three trapped particles.

The full simulation of the interparticle forces in our experiment, with multiple particles and the fields due to the evanescent tail of the mode in the photonic crystal, is computationally expensive. However, we believe that a simplified model with a plane wave source in water can provide some insight. Figure 18 shows the potential energy surfaces [101] computed for one, two and three 200 nm gold particles under plane wave illumination in water ($n = 1.318$). Each position on the plot represents the in-plane optical potential experienced by a 200 nm Au particle whose center is at that location. The refractive index of gold was taken from Johnson & Christy [105]. The smaller white circles represent the positions of the holes along the diagonals of the photonic crystal lattice, and are merely a guide to the eye (there is no silicon photonic crystal slab in this simulation). The larger, filled-in circles represent the positions of the particles (the size is larger than 200 nm to avoid overlap). In each case the incident plane wave is polarized

along the x-direction, and has a wavelength of 1550 nm. The colorbar is in arbitrary units of potential in the lateral direction, with the maximum value in each case set to 0.

From our experiments, as well as the force map in Figure 17, we observe that particles are trapped above the holes of the photonic crystal. However, interparticle interactions place a further constraint on the stability of these traps. In Figure 18a, we see potential wells overlapping with holes just above and below the trapped particle. Of the eight holes closest to the trapped particle, only these two correspond to stable positions in this simplified system. Next, we place a second trapped particle in one of these holes and repeat the potential energy surface calculation (Figure 18b). Again, of the ten holes which are within one lattice constant of the trapped particles, only the two above and below are stable. Performing the simulations with a third trapped particle (Figure 18c), we again observe the same trend – particles are much more likely to be trapped in holes along the chain's axis than in other holes within the photonic crystal. Although the photonic crystal slab is not present in this experiment, we believe that this simplified model of the interparticle interactions is nonetheless relevant to the actual experimental conditions.

3.5 – Discussion

In summary, we have presented the first demonstration of the LATS method for self assembly of gold nanoparticles. We observe that strong interparticle interactions lead to the emergence of self-stabilizing, 1D particle chains within the 2D periodic potential of the optical field. The emergence of nanoparticle patterns due to cooperative behavior is an intriguing area for future research. Since both particle-template and particle-particle interactions scale with incident intensity, these competing effects are fundamentally inseparable. Exploration of how the template might be redesigned to give rise to other nanoparticle patterns (such as regular, 2D arrays) is ongoing in our laboratory, and is particularly intriguing in the context of mixed metal / dielectric particle systems [81, 100]. An understanding of the physics of such strongly coupled, multi-particle systems may even yield insight into other cases of pattern formation within a 2D periodic potential, such as the formation of defects within layer-by-layer atomic growth methods.

3.6 – Methods

The fabrication of devices followed a similar process as that described in Chapter one. The experimental set-up was modified by replacing the 20X objective with a $f = 30$ mm focal length aspheric lens.

Stiffness analysis. The stiffness analysis of the traps was similar to that described in Chapter two. However, given the larger beam size, the power per trap was taken to be $11.9 \mu\text{W}$, which represents the average value within the $1/e^2$ radius of the Gaussian beam intensity. Because a cluster did not form, we could not be certain of the exact position of the beam and thus the power at any given site.

Stability of trapped particles. We processed a time-lapse video that was 1990 frames in length, taken at a rate of 1 frame per second, and thus representing more than 30 minutes of trapping

time. During the entire video, the polarization was aligned with a diagonal of the square lattice. For each frame, and for each trapped particle, it was determined whether or not that particle was part of a chain.

Chapter 4 – Optical Brownian Ratchet

4.1 – Introduction

The basic concept behind Brownian ratchets is illustrated in Figure 19. A periodic, asymmetric potential is used to bias the Brownian motion of particles in solution in a particular direction. When the potential is on, particles fall downhill into the potential minima. When the potential is off, particles diffuse randomly via Brownian motion. By carefully selecting the frequency and duty cycle of the flashing potential, the net motion of particles will be predominantly in one direction. Brownian ratchets are interesting both for their ability to rectify motion from random processes, and because they mimic motor protein assemblies and other molecular scale biological processes [106].

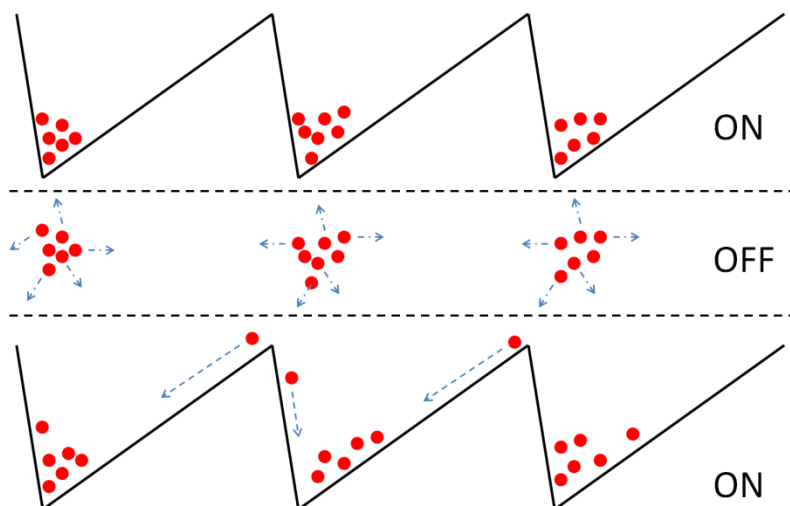


Figure 19. Schematic of “on-off Brownian ratchet.” When the potential is on, particles fall into the potential minima. When the potential is off, particles diffuse randomly via Brownian motion. The asymmetry of the potential ensures that particles can only move in one direction only (to the left, in this case) when the potential is turned back on.

So-called on-off Brownian ratchets [107] have been realized in a variety of systems. Rousselet *et al.* [108] used a series of interleaved “Christmas tree” electrodes to apply the

asymmetric potential, which was used to rectify the motion of sub-micron sized polystyrene spheres. Their system achieved a maximum velocity of $1 \mu\text{m/s}$. Faucheux *et al.* [109] realized an on-off Brownian ratchet optically by combining a standard optical tweezers set-up with oscillating mirrors and a periodic, asymmetric spatial modulation of the trap strength. $1.5 \mu\text{m}$ diameter polystyrene spheres were observed to move in the forward direction only. Gorre-Talini *et al.* [110] used a high-frequency electric field with a blazed optical grating to generate the asymmetric potential, then demonstrated size-based sorting of polystyrene particles due to regimes of positive and negative dielectrophoresis. These regimes correlated with the sign of the real part of the polarizability of the particle, which in turned depended upon the frequency of the signal. Operating at a frequency just above the crossover frequency for large particles, but below the crossover frequency for smaller particles, allowed the authors to propel the two different sizes in opposite directions. Bader *et al.* [111] and Hammond *et al.* [112] used the interdigitated electrode scheme to rectify the motion of DNA as small as 25 base-pairs.

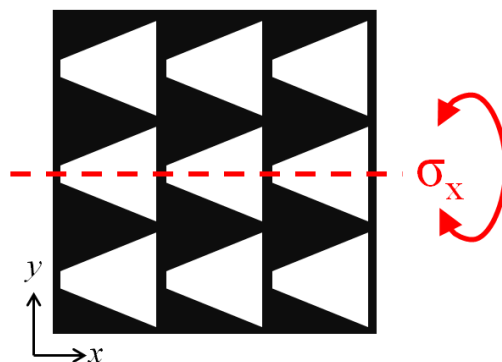


Figure 20. 3x3 array of asymmetric unit cells in a photonic crystal lattice. Mirror symmetry along x-axis only implies that there will be no net motion of particles in the y-direction. Black represents silicon and white represents water.

4.2 – Device Design

To achieve an asymmetric unit cell in a photonic crystal, the hole shape cannot be circular. The most straightforward choice is a triangular hole, which preserves mirror symmetry in one direction through the unit cell but not the other. The structure with triangular holes is symmetric with respect to the x -axis but not to the y -axis. A 3D-FDTD simulation of this device is shown in Figure 21. The lattice has the following parameters: 850 nm lattice constant, triangle height of 750 nm, triangle base of 750 nm, and silicon device layer thickness of 250 nm. Figure 21a shows the simulated normal incidence transmission spectrum, indicating the excitation of two guided resonance modes. The E^2 profile for each of these modes is shown in Figures 21b and 21c.

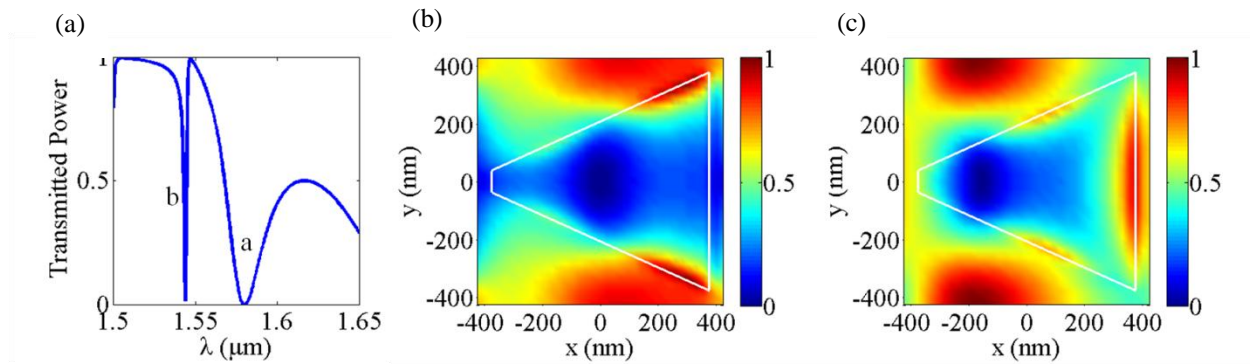


Figure 21. Photonic crystal rectangular lattice with asymmetric unit cell. (a) Transmission spectrum simulated via 3D-FDTD showing two guided resonance modes labeled “a” and “b.” (b) E^2 profile in one unit cell of mode labeled “b” in (a). (c) E^2 profile of mode labeled “a” in (a).

4.3 – Force and Potential Calculations

Forces acting on a 520 nm polystyrene particle whose lower edge was 40 nm from the surface of the device were calculated for the mode “b” using the Maxwell stress tensor method described in Chapter one. (By examining the x -cuts of the potential through the minima for the

two modes, I determined that mode “b” had more asymmetry and thus was more suitable for use as a Brownian ratchet.) Figure 22 shows the forces and potential for this mode in one unit cell of the photonic crystal lattice. In Figure 22a, the background and colorbar represent the vertical force, where a negative value of force indicates attraction toward the slab. The arrows represent the magnitude and direction of the in-plane forces. The strongest vertical force is near $x = 200$ nm along the boundary between neighboring unit cells, and is also the only stable point when considering the in-plane forces. This can be seen by examining Figure 22b, which shows the in-plane optical potential in one unit cell (obtained by integrating the in-plane forces). An x -cut through the potential minimum (at the upper/lower boundary of the unit cell) is shown in Figure 22c. (The x -cut for mode “a” is not shown.) Figure 22d shows the full in-plane potential as a surface in three dimensions. The black background was added for ease of viewing.

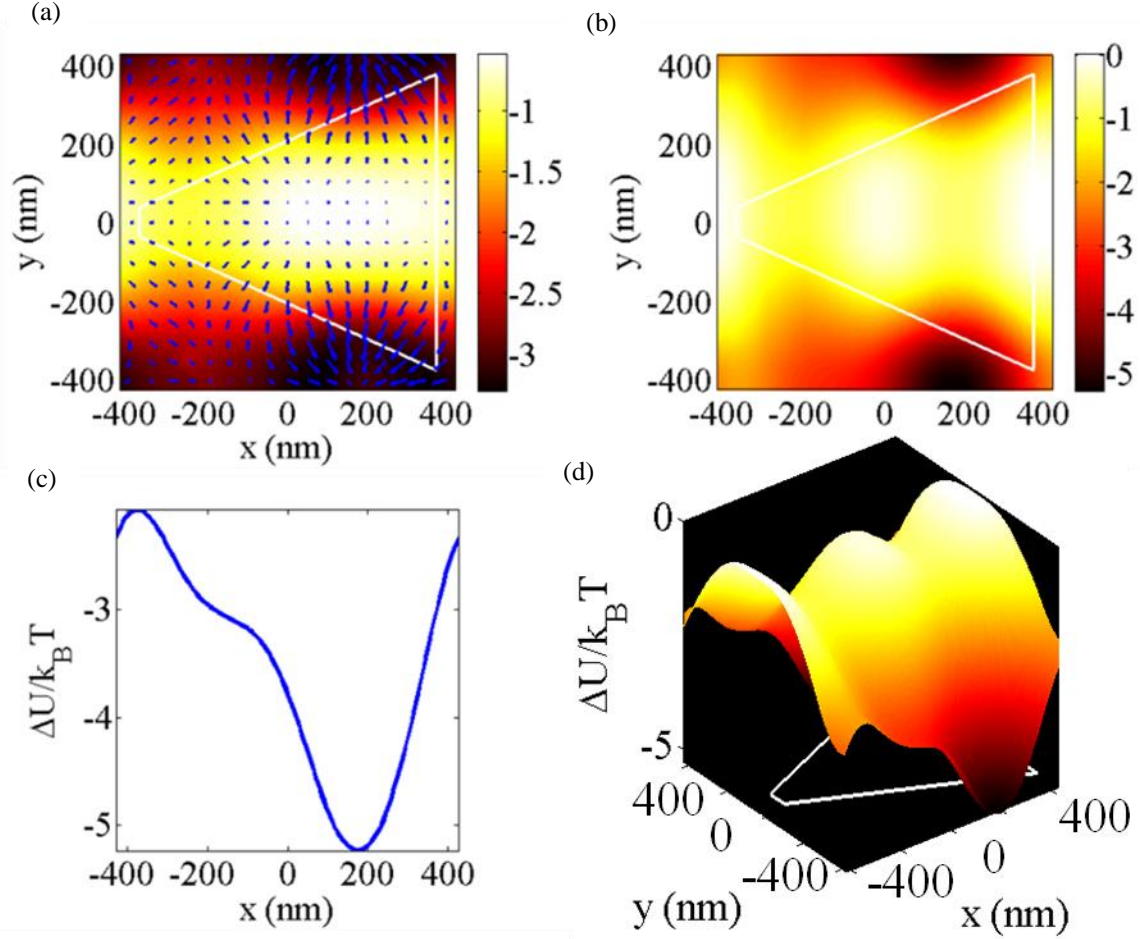


Figure 22. Forces and potential for the mode labeled “b” in Figure 21. All forces in the normalized, dimensionless parameter Fc/P , where P is the incident power. (a) Forces calculated via Maxwell stress tensor formalism. The background and colorbar represent the vertical force, where a negative force indicates attraction toward the slab. The arrows represent the magnitude and direction of the in-plane forces. (b) In-plane optical potential calculated by integrating the in-plane forces in (a). (c) An x -cut through the potential minimum showing strong asymmetry. (d) The full in-plane potential represented as a surface in three dimensions.

The probability of a particle moving forward or backward in an on-off ratchet depends strongly upon the temporal periodicity of the potential. This forward probability is expressed as [109]:

$$P_f = \frac{1}{2} \text{Erfc} \left(\frac{\ell_f}{\sqrt{4D\tau_{off}}} \right)$$

where $\text{Erfc}(x) = \frac{2}{\sqrt{\pi}} \int_x^\infty e^{-t^2} dt$ is the complement of the error function, ℓ_f is the distance from the potential minimum to the potential maximum in the forward direction, D is the diffusion coefficient of the particle in the medium, and τ_{off} is the amount of time that the potential is off during one cycle. A similar expression exists for the probability of the particle moving backward. Figure 23a shows plots of these probabilities as a function of τ_{off} , using the asymmetry factor of 1.83 from the simulations in Figure 21. The measured value of the diffusion coefficient, $0.56 \mu\text{m}^2/\text{s}$, from Chapter two was used. Figure 23b shows the difference between these probabilities, which indicates an optimal value of τ_{off} of just under 200 ms, i.e. a temporal frequency of 5 Hz, which can easily be achieved with or a function generator or even a mechanical chopper. This value of τ_{off} may allow for particles to escape from their traps, so it may need to be adjusted.

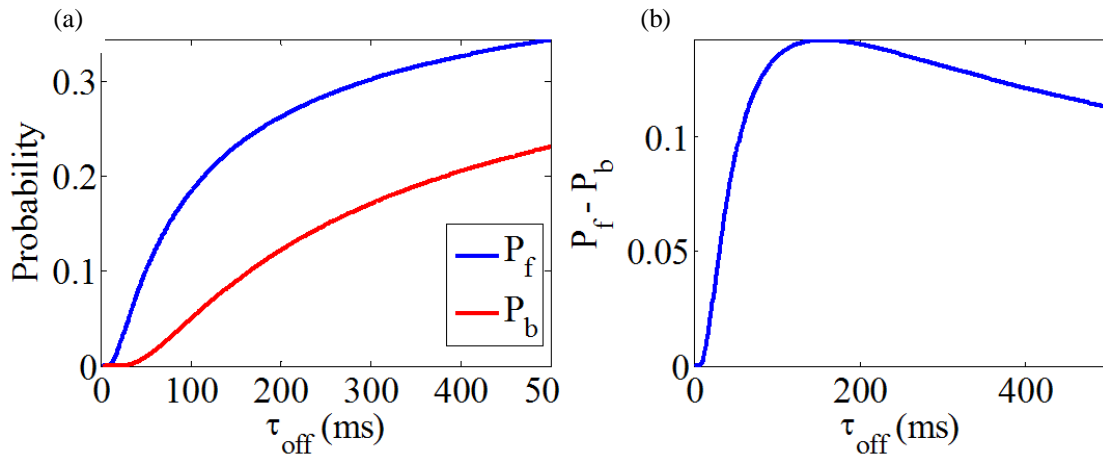


Figure 23. Probability of net motion as a function of τ_{off} . a) Probability of moving forward and backward using parameters extracted from the optical potential calculations in Figure 22. b) Probability of moving forward minus probability of moving backward, indicating an optimal value of τ_{off} .

I fabricated the devices designed above using the standard e-beam exposure and etching methods described in Chapter one. Scanning electron micrograph images of the device are

shown in Fig. 24a. The device has the following parameters: lattice constant = 850 nm, triangle base = 700 nm, triangle height = 700 nm, device layer height = 250 nm. The device was mounted in the experimental set-up, and the transmission spectrum in Fig. 24b was acquired. The coupling was over 90%, and the Q factor extracted from the spectrum was near 1500.

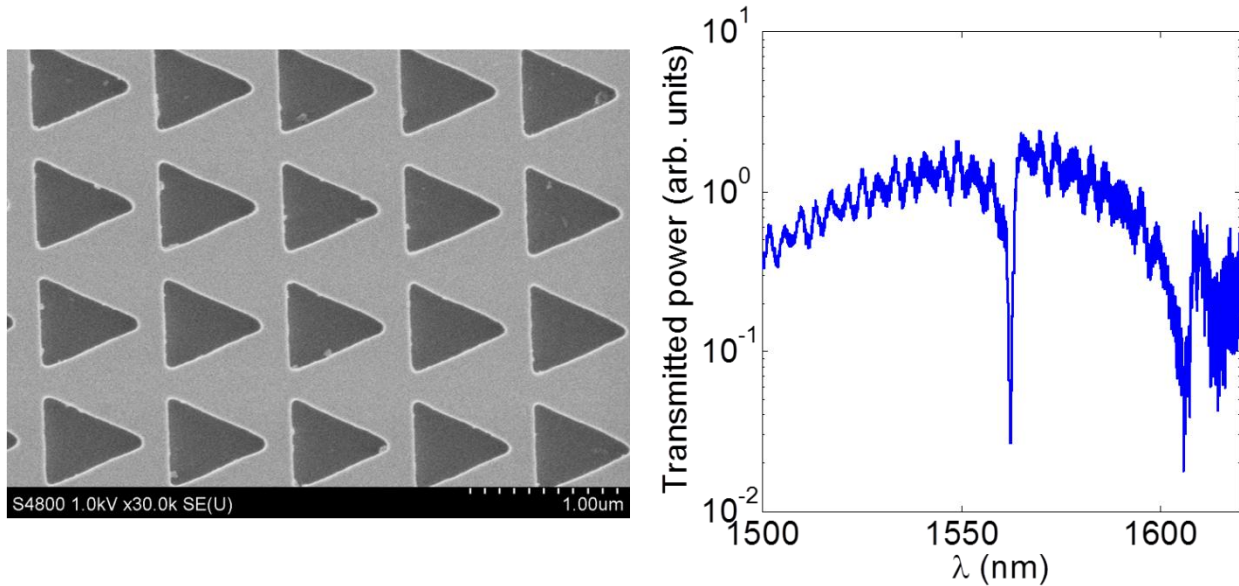


Figure 24. Ratchet device characterization. (a) Scanning electron microscope image of the sample fabricated in the SOI platform. (b) Measured transmission spectrum of the device.

To perform the ratchet experiment, the first step is to trap a few particles. After this the laser would then be modulated with a simple square wave, and the particles' motion would be observed. However, I did not observe any trapping with this device. I prepared the sample for trapping with 520 nm polystyrene particles and a 5 μm high microfluidic channel. I repeated this experiment across multiple days and multiple devices (with similar parameters). In each case the coupling to the mode was high, which indicates that the mode was excited. Many particles were observed in the trapping region but did not become trapped at any point.

I believe this inability to trap particles is due to the spatial variation of the mode. In Fig. 21 we see that the highest intensity occurs above the silicon area. Even though particles should be

attracted to this region of highest intensity, there is no additional geometrical confinement due to the sinking of the particle into the hole, as was the case in the experiments of Chapters two and three. In these devices, the field was largely concentrated in the hole, and as a result the vertical force was strongest there. Furthermore, the in-plane forces also pointed toward the center of the hole, and the combination of these two factors led to stable trapping.

4.4 – Device Re-design

Given this experience, I re-designed the ratchet device. The goal was to find a mode with a large field intensity in the holes while still maintaining a sawtooth-type potential profile along one direction of the lattice. This sawtooth profile should naturally be taken through the center of the triangle along its height (shown as the x -direction in Figs. 21-22). I found such a mode in the spectrum of the previous devices, but its resonant wavelength was outside the range of our laser and EDFA, and thus would not be practical for the current experiment.

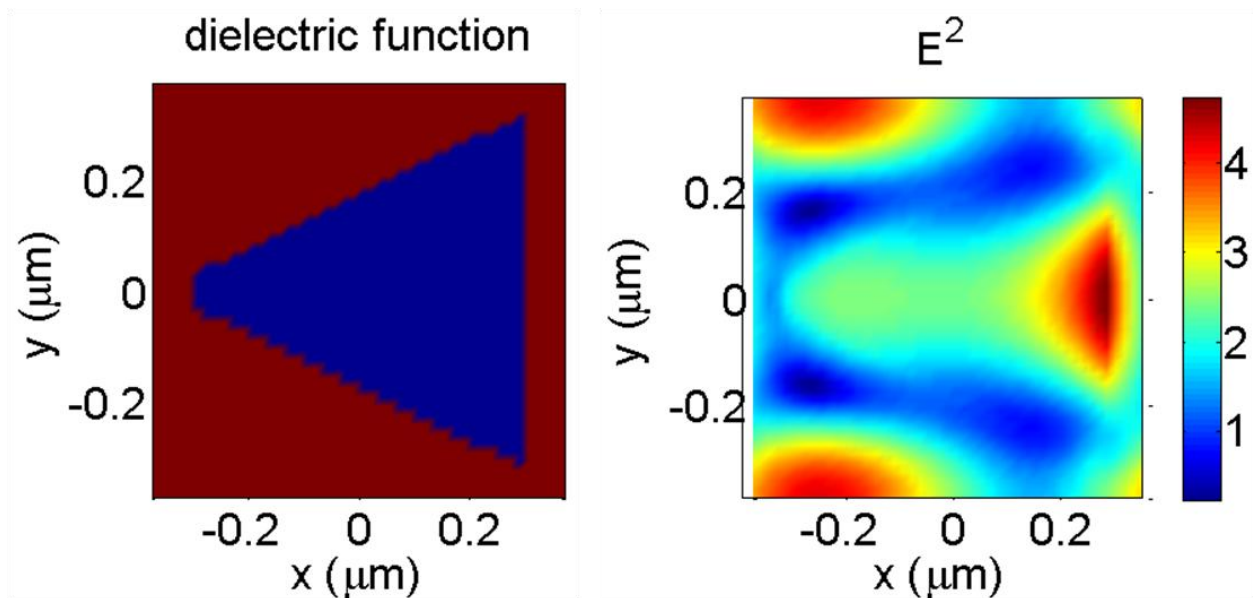


Figure 25. Redesign of ratchet device. (a) Dielectric function. Red represents silicon and blue represents water. (b) E^2 profile in one unit cell.

In order to move this mode into the correct range, I re-designed the lattice to have the following parameters: lattice constant = 750 nm, triangle height = 600 nm, triangle base = 640 nm, and device layer height = 250 nm. The simulation results for this device are shown in Fig. 25. We can observe in Fig. 25b that there is a relatively higher amount of field intensity near the hole.

I believe that this project may yield interesting results. However, I was unable to proceed any further because of equipment failure. Although I created the patterns for the redesigned devices, the electron beam system went offline and remained offline for several months. I am hopeful that my colleagues may pick up this project from this point. This mode should at least offer the ability to trap the particles. From there it should be a straightforward matter to test the ratcheting behavior. By adjusting the modulation frequency, it should be possible to identify regions in which the cluster remains trapped (higher frequencies) and regions in which trapping does not occur (lower frequencies). I expect that the best procedure would be trap a cluster with no modulation or at a high modulation frequency. Then, the frequency should gradually be lowered to the transition frequency and adjusted slightly below that value while monitoring the results on the camera.

Chapter 5 – Future Work

5.1 – Assembly of a regular array of metallic particles

A version of this section was published as reference [121], with further submissions in progress.

The LATS technique has various possibilities and applications – those listed here are but a few. Given the results from Chapter three on metal chains, it is natural to ask if regular, 2D clusters of metallic particles can be formed using LATS. The initial goal of the work in Chapter three was in fact to assemble such a cluster, and the resulting chains were somewhat of a surprise. The inability to form clusters was ascribed to the interparticle interactions, and specifically to scattering of the metallic particles and the resulting forces due to the interference of the scattered light and the electromagnetic mode supported by the photonic crystal slab.

After attempting to assemble regular metallic clusters with square symmetry using a variety of sizes of particles, lattice constants, and even lattice types (i.e. lattices whose underlying square symmetry was preserved while perturbing certain hole sizes), we tried a similar experiment but in a lattice with hexagonal symmetry. Preliminary results were reported at CLEO in 2014 [113] and are summarized here. The full results are currently in preparation for submission. My colleague Ningfeng Huang is the lead author on this paper.

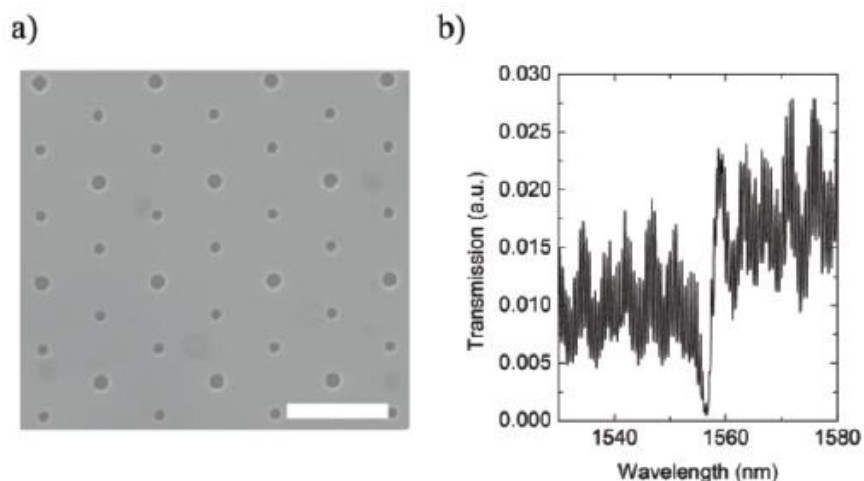


Figure 26. Device for assembly of 2D nanoparticle array. (a) SEM image of device. (b) Transmission spectrum of device showing mode near 1550 nm.

Figure 26a shows a scanning electron micrograph image of the device. It is based on the triangular lattice, but features perturbed hole sizes in the form of a graphite lattice. The quality factor of the mode in figure 26b is approximately 800. As can be seen in figure 27, we were indeed able to assemble a regular 2D array of metallic particles with this lattice.

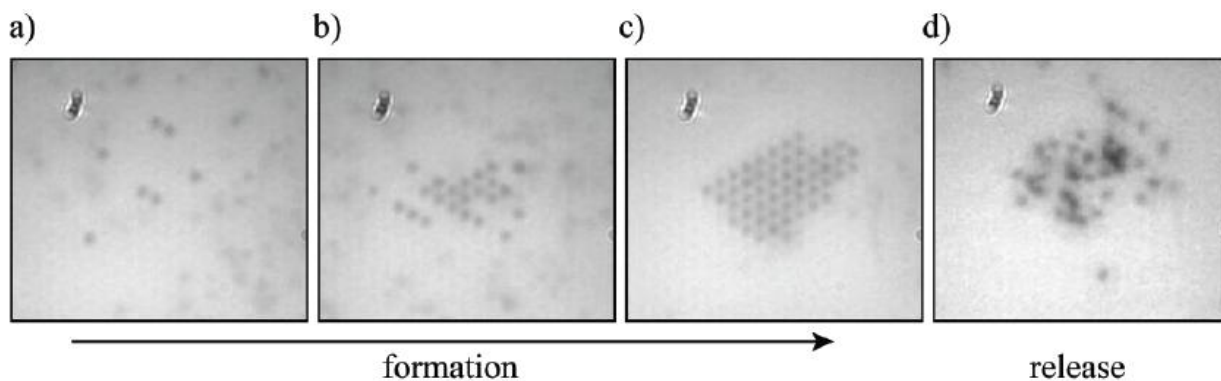


Figure 27. Assembly of a 2D array of 200 nm Au particles. Frames (a) through (c) show the evolution of the cluster over time. Frame (d) shows the release of the particles upon blocking of the beam. The mark in the upper left-hand corner of each image is a dust particle on the camera detector surface.

5.2 – Solidification of assembled arrays

The arrays of particles created via LATS can be viewed as photonic crystals. The ability to carefully choose the material and lattice constant of the array offers flexibility for designing the resulting structure [65]. Although it is possible to optically measure the arrays in situ, the ability to transfer the assembled array to another substrate would enable LATS to be viewed as a fabrication technique, capable of producing single-layer photonic crystals for use in other applications. Assembly and transfer of metallic arrays would enable the study of narrow plasmon resonances that result from the coupling of localized surface plasmons and grating diffraction orders, such as those studied in [91, 92, 114-116]. Furthermore, in each of these papers the authors using a deposition process to form the elements of the metallic array. The resulting elements are necessarily disk-shaped, whereas the LATS technique would enable the assembly of perfectly-periodic arrays of nanospheres. The plasmonic properties of a metallic nanoparticle depend sensitively upon size [117], and thus this would represent a potentially fruitful direction for further studies.

In order to transfer the assembled arrays, they must first be solidified in place. A variety of UV-curable polymers and resins exist which could be used as the solvent in the LATS experiment, or used to dilute the aqueous solution of particles. A UV laser and high-intensity lamp could then be used to cross-link the polymer matrix which would solidify the assembled array in place. Similar techniques have been successfully applied in [118, 119]. Care would need to be taken to account for the change in refractive index due to the presence of the polymer in the particle solution, as well as the resulting structure in the embedded matrix. If successful this transfer technique should extend the utility of LATS for fabricating bottom-up materials.

Chapter 6 – Conclusion

In this thesis we have successfully demonstrated the technique that we call light-assisted, templated self assembly. In the first demonstration we successfully trapped an array of 520 nm polystyrene particles above a square lattice. The number of particles trapped was well above 100, and could be increased by using a larger beam or a mode with a larger quality factor. The traps were characterized using standard techniques and were found to have stiffness values comparable to those reported elsewhere in the literature for single-particle traps. The system behaved as an array of non-interacting optical traps, with each trap positioned above the hole in each unit cell of the square lattice. Although other techniques exist for trapping arrays of particles, they typically require a spatial light modulator and fast-scanning mirrors. Our technique requires just a simple, Gaussian input beam.

Next we repeated the LATS technique but with metallic particles. Our expectation was that the technique would either work – namely that we would trap an array of the metallic particles – or it would not work. Instead, we found an intermediate case involving the emergence of one-dimensional particle chains trapped in a two-dimensionally periodic potential due to the mode in the slab. The chains were observed to align in the direction opposite to the incident polarization of the beam. The particles in chains were self-stabilizing in the sense that these particles persisted much longer than other particles that were trapped in isolated positions. We explained these results by using a simplified model of the particle scattering in the absence of the slab. The system is best understood as a competition between particle-template and particle-particle interactions.

The LATS system can also be used as a Brownian ratchet. By designing the unit cell to have an asymmetric potential profile along one direction of the lattice, we can rectify the motion of

particles in solution simply by turning the beam on and off. Several devices were fabricated with such asymmetric unit cells, and their transmission spectra agreed with simulations.

The bottom-up technique for assembling materials described in this thesis offer promise for future integrated applications. Although techniques exist for assembling arrays in free space, they require bulky optics and are thus not suitable for on-chip applications. An assembled array of particles could serve, for example, as a reversible optical filter which passes light for certain frequencies or polarizations, and reflects light for others. Furthermore, by using a photonic crystal laser as the light source, thereby merging the source and the traps, ultimate miniaturization should be possible. It is my sincere hope that the research presented in this thesis will lay the ground work for future studies of novel optical devices fabricated via LATS.

References

1. Kepler, J., in *De Cometis libelli tres*. 1619 Augsburg.
2. Maxwell, J.C., *A treatise on electricity and magnetism*. Vol. 1. 1881: Clarendon press.
3. Lebedev, P., *Experimental examination of light pressure*. *Annalen der Physik*, 1901. **6**: p. 433.
4. Nichols, E.F., & Hull, G. F., *A preliminary communication on the pressure of heat and light radiation*. *Physical Review (Series I)*, 1901. **13**: p. 307-320.
5. Nichols, E.F., & Hull, G. F., *The pressure due to radiation*. *Physical Review (Series I)*, 1903. **17**: p. 26-50.
6. Ashkin, A., Dziedzic, J. M., Chu, S., *Observation of a single-beam gradient force optical trap for dielectric particles*. *Optics Letters*, 1986. **11**: p. 288-290.
7. Ashkin, A., Dziedzic, J. M., Tamane, T., *Optical trapping and manipulation of single cells using infrared laser beams*. *Nature*, 1987. **330**: p. 769-771.
8. Svoboda, K. and S.M. Block, *Optical trapping of metallic Rayleigh particles*. *Optics Letters*, 1994. **19**(13): p. 930-932.
9. Sato, S., Y. Harada, and Y. Waseda, *Optical trapping of microscopic metal particles*. *Optics Letters*, 1994. **19**(22): p. 1807-1809.
10. Furukawa, H. and I. Yamaguchi, *Optical trapping of metallic particles by a fixed Gaussian beam*. *Optics Letters*, 1998. **23**(3): p. 216-218.
11. Ke, P.C. and M. Gu, *Characterization of Trapping Force on Metallic Mie Particles*. *Applied Optics*, 1999. **38**(1): p. 160-167.
12. O'Neil, A.T. and M.J. Padgett, *Three-dimensional optical confinement of micron-sized metal particles and the decoupling of the spin and orbital angular momentum within an optical spanner*. *Optics Communications*, 2000. **185**(1): p. 139-143.
13. Link, S. and M.A. El-Sayed, *Optical properties and ultrafast dynamics of metallic nanoparticles*. *Annual Review of Physical Chemistry*, 2003. **54**(1): p. 331-366.
14. Hansen, P.M., et al., *Expanding the Optical Trapping Range of Gold Nanoparticles*. *Nano Letters*, 2005. **5**(10): p. 1937-1942.
15. Bosanac, L., et al., *Efficient Optical Trapping and Visualization of Silver Nanoparticles*. *Nano Letters*, 2008. **8**(5): p. 1486-1491.
16. Wang, M.D., et al., *Stretching DNA with optical tweezers*. *Biophysical Journal*, 1997. **72**(3): p. 1335-1346.
17. Bustamante, C., Z. Bryant, and S.B. Smith, *Ten years of tension: single-molecule DNA mechanics*. *Nature*, 2003. **421**(6921): p. 423-427.
18. Block, S.M., D.F. Blair, and H.C. Berg, *Compliance of bacterial flagella measured with optical tweezers*. *Nature*, 1989. **338**(6215): p. 514-518.
19. Bustamante, C., D. Keller, and G. Oster, *The physics of molecular motors*. *Accounts of chemical research*, 2001. **34**(6): p. 412-420.
20. Block, S.M., L.S.B. Goldstein, and B.J. Schnapp, *Bead movement by single kinesin molecules studied with optical tweezers*. *Nature*, 1990. **348**(6299): p. 348-352.
21. Corbitt, T., et al., *An All-Optical Trap for a Gram-Scale Mirror*. *Physical Review Letters*, 2007. **98**(15): p. 150802.
22. Safavi-Naeini, A.H., et al., *Squeezed light from a silicon micromechanical resonator*. *Nature*, 2013. **500**(7461): p. 185-189.
23. Kawata, S. and T. Sugiura, *Movement of micrometer-sized particles in the evanescent field of a laser beam*. *Optics Letters*, 1992. **17**.
24. Kawata, S. and T. Tani, *Optically driven Mie particles in an evanescent field along a channel waveguide*. *Optics Letters*, 1996. **21**: p. 1768-1770.

25. Reece, P.J., Garcés-Chavéz, V., Dholakia, K., *Near-field optical micromanipulation with cavity enhanced evanescent waves*. Applied Physics Letters, 2006. **88**: p. 221116.
26. Quidant, R., D. Petrov, and G. Badenes, *Radiation forces on a Rayleigh dielectric sphere in a patterned optical near field*. Optics Letters, 2005. **30**(9): p. 1009-1011.
27. Anderson, M.S. and W.T. Pike, *A Raman-atomic force microscope for apertureless-near-field spectroscopy and optical trapping*. Review of Scientific Instruments, 2002. **73**(3): p. 1198-1203.
28. Yang, A.H.J., et al., *Optical manipulation of nanoparticles and biomolecules in sub-wavelength slot waveguides*. Nature, 2009. **457**: p. 71-75.
29. Mandal, S., X. Serey, and D. Erickson, *Nanomanipulation using silicon photonic crystal resonators*. Nano Lett., 2010. **10**: p. 99-104.
30. Serey, X., Mandal, S., Erickson, D., *Comparison of silicon photonic crystal resonator designs for optical trapping of nanomaterials*. Nanotechnology, 2010. **21**: p. 305202.
31. Erickson, D., Serey, X., Chen, Y.-F., Mandal, S., *Nanomanipulation using near field photonics*. Lab on a Chip, 2011. **11**: p. 995-1009.
32. Lin, S., Crozier, K. B., *Trapping-assisted sensing of particles and proteins using on-chip optical microcavities*. ACS Nano, 2013. **7**: p. 1725-1730.
33. Lin, S., Zhu, W., Jin, Y., & Crozier, K. B., *Surface-enhanced Raman scattering with Ag nanoparticles optically trapped by a photonic crystal cavity*. Nano Letters, 2013. **13**: p. 559-564.
34. Lin, S., E. Schonbrun, and K. Crozier, *Optical manipulation with planar silicon microring resonators*. Nano Lett., 2010. **10**: p. 2408-2411.
35. Lin, S. and K.B. Crozier, *Planar silicon microrings as wavelength-multiplexed optical traps for storing and sensing particles*. Lab on a Chip, 2011. **11**(23): p. 4047-4051.
36. Teich, M.C. and B. Saleh, *Fundamentals of photonics*. Canada, Wiley Interscience, 1991: p. 3.
37. Visscher, K., Brakenhoff, G.J. & Krol, J.J., *Micromanipulation by "multiple" optical traps created by a single fast scanning trap integrated with the bilateral confocal scanning laser microscope*. Cytometry, 1993. **14**: p. 105-114.
38. Visscher, K., S.P. Gross, and S.M. Block, *Construction of multiple-beam optical traps with nanometer-resolution position sensing*. Selected Topics in Quantum Electronics, IEEE Journal of, 1996. **2**(4): p. 1066-1076.
39. Visscher, K., and Block, S.M., *Versatile optical traps with feedback control*. Methods in Enzymology, 1998. **298**: p. 460-489.
40. Vossen, D.L.J., et al., *Optical tweezers and confocal microscopy for simultaneous three-dimensional manipulation and imaging in concentrated colloidal dispersions*. Review of Scientific Instruments, 2004. **75**(9): p. 2960-2970.
41. Dufresne, E.R. and D.G. Grier, *Optical tweezer arrays and optical substrates created with diffractive optics*. Review of Scientific Instruments, 1998. **69**(5): p. 1974-1977.
42. Liesener, J., et al., *Multi-functional optical tweezers using computer-generated holograms*. Optics Communications, 2000. **185**(1): p. 77-82.
43. Dufresne, E.R., et al., *Computer-generated holographic optical tweezer arrays*. Review of Scientific Instruments, 2001. **72**(3): p. 1810-1816.
44. Korda, P., Spalding, G. C., Dufresne, E. R., Grier, D. G., *Nanofabrication with holographic optical tweezers*. Review of Scientific Instruments, 2002. **73**: p. 1956-1957.
45. Korda, P.T., G.C. Spalding, and D.G. Grier, *Evolution of a colloidal critical state in an optical pinning potential landscape*. Physical Review B, 2002. **66**(2): p. 024504.
46. MacDonald, M.P., Spalding, G. C., Dholakia, K., *Microfluidic sorting in an optical lattice*. Nature, 2003. **426**: p. 421-424.
47. Grier, D.G. and Y. Roichman, *Holographic optical trapping*. Applied Optics, 2006. **45**(5): p. 880-887.
48. Reicherter, M., et al., *Optical particle trapping with computer-generated holograms written on a liquid-crystal display*. Optics Letters, 1999. **24**(9): p. 608-610.

49. Burns, M.M., J.-M. Fournier, and J.A. Golovchenko, *Optical binding*. Physical Review Letters, 1989. **63**: p. 1233-1236.
50. Burns, M.M., Fournier, J.-M., Golovchenko, J. A., *Optical matter: Crystallization and binding in intense optical fields*. Science, 1990. **249**: p. 749-754.
51. Tatarkova, S.A., A.E. Carruthers, and K. Dholakia, *One-Dimensional Optically Bound Arrays of Microscopic Particles*. Physical Review Letters, 2002. **89**(28): p. 283901.
52. Mellor, C.D. and C.D. Bain, *Array Formation in Evanescent Waves*. ChemPhysChem, 2006. **7**(2): p. 329-332.
53. Mellor, C.D., T.A. Fennerty, and C.D. Bain, *Polarization effects in optically bound particle arrays*. Optics Express, 2006. **14**: p. 10079-10088.
54. Taylor, J.M., et al., *Emergent properties in optically bound matter*. Optics Express, 2008. **16**: p. 6921-6929.
55. Wong, L. and C. Bain. *Optical trapping and binding in evanescent optical landscapes*. in *SPIE NanoScience+Engineering*. 2009: International Society for Optics and Photonics.
56. Demergis, V. and E.-L. Florin, *Ultrastrong Optical Binding of Metallic Nanoparticles*. Nano Letters, 2012. **12**: p. 5756-5760.
57. Jackson, J.D., *Classical Electrodynamics (3rd ed.)*. Wiley, 1999, 1999.
58. Svoboda, K., *Biological applications of optical forces*. Annual Review of Biophysics and Biomolecular Structure, 1994. **23**: p. 247-285.
59. Neuman, K.C., Block, S. M., *Optical trapping*. Review of Scientific Instruments, 2004. **75**: p. 2787-2808.
60. Faxén, H., *Der Widerstand gegen die Bewegung einer starren Kugel in einer zähen Flüssigkeit, die zwischen zwei parallelen ebenen Wänden eingeschlossen ist*. Annalen der Physik, 1922. **373**(10): p. 89-119.
61. Reynolds, O., *An Experimental Investigation of the Circumstances Which Determine Whether the Motion of Water Shall Be Direct or Sinuous, and of the Law of Resistance in Parallel Channels*. Philosophical Transactions of the Royal Society of London, 1883. **174**: p. 935-982.
62. Segelstein, D.J., *The complex refractive index of water*. 2011, University of Missouri--Kansas City.
63. Juan, M.L., Righini, M., Quidant, R., *Plasmon nano-optical tweezers*. Nature Photonics, 2011. **5**: p. 349-356.
64. Whitesides, G.M., Grzybowski, B., *Self-assembly at all scales*. Science, 2002. **295**: p. 2418.
65. Xia, Y., Gates, B. & Li, Z.-Y., *Self-assembly approaches to three-dimensional photonic crystals*. Advanced Materials, 2001. **13**(6): p. 409-413.
66. Vlasov, Y.A., Bo, X.-Z., Sturm, J.C. & Norris, D.J., *On-chip natural assembly of silicon bandgap crystals*. Nature, 2001. **414**(6861): p. 289.
67. Vlasov, Y.A., et al., *On-chip natural assembly of silicon photonic bandgap crystals*. Nature, 2001. **414**(6861): p. 289-293.
68. Yin, Y., Lu, Y., Gates, B. & Xia, Y., *Template-assisted self-assembly: a practical route to complex aggregates of monodispersed colloids with well-defined sizes, shapes and structures*. Journal of the American Chemical Society, 2001. **123**: p. 8718-8729.
69. Holzner, F., et. al., *Directed placement of gold nanorods using a removable template for guided assembly*. Nano Letters, 2011. **11**: p. 3957-3062.
70. Lee, I., Zheng, H., Rubner, M.F. & Hammond, P.T., *Controlled cluster size in patterned particle arrays via directed adsorption on confined surfaces*. Advanced Materials, 2002. **14**: p. 572-577.
71. Kim, Y.H., Park, J., Yoo, P.J. & Hammond, P.T., *Selective assembly of colloidal particles on a nanostructured template coated with polyelectrolyte multilayers*. Advanced Materials, 2007. **19**: p. 4426-4430.
72. Liu, S., Maoz, R., Schmid, G. & Sagiv, J., *Template guided self-assembly of [Au55] clusters on nanolithographically defined monolayer patterns*. Nano Letters, 2002. **2**: p. 1055-1060.

73. von Blaaderen, A., Ruel, R. & Wiltzius, P., *Template-directed colloidal crystallization*. Nature, 1997. **385**: p. 321-324.
74. Ilievski, F., Mirica, K.A., Ellerbee, A.K. & Whitesides, G.M., *Templated self-assembly in three dimensions using magnetic levitation*. Soft Matter, 2011. **7**: p. 9113-9118.
75. Henry, M.D., Walavalkar, S., Homyk, A. & Scherer, A., *Alumina etch masks for fabrication of high-aspect-ratio silicon micropillars and nanopillars*. Nanotechnology, 2009. **20**: p. 255305-255309.
76. Koschwanetz, J.H., R.H. Carlson, and D.R. Meldrum, *Thin PDMS films using long spin times or tert-butyl alcohol as a solvent*. PLoS ONE, 2009. **4**(2): p. e4572.
77. Jaquay, E., et al., *Light-assisted, templated self-assembly using a photonic-crystal slab*. Nano Letters, 2013. **13**: p. 2290-2294.
78. Fan, S. and J.D. Joannopoulos, *Analysis of guided resonances in photonic crystal slabs*. Phys. Rev. B, 2002. **65**: p. 235112.
79. Mejia, C.A., A. Dutt, and M.L. Povinelli, *Light-assisted templated self-assembly using photonic crystal slabs*. Optics Express, 2011. **19**: p. 11422-11428.
80. Ma, J., Martínez, L. J., Povinelli, M. L., *Optical trapping via guided resonance modes in a slot-Suzuki-phase photonic crystal lattice*. Opt. Express, 2012. **20**: p. 6816-6824.
81. Mejia, C.A., N. Huang, and M.L. Povinelli, *Optical trapping of metal-dielectric nanoparticle clusters near photonic crystal microcavities*. Optics Letters, 2012. **37**: p. 3690-3692.
82. Padgett, M., Di Leonardo, R., *Holographic optical tweezers and their relevance to lab on chip devices*. Lab on a Chip, 2011. **11**: p. 1196-1205.
83. Dholakia, K. and P. Zemanek, *Gripped by light: Optical Binding*. Reviews of Modern Physics, 2010. **82**: p. 1767-1791.
84. Juan, M.L., Gordon, R., Pang, Y., Eftekhari, F., Quidant, R., *Self-induced back-action optical trapping of dielectric nanoparticles*. Nature Physics, 2009. **5**: p. 915-919.
85. Ladavac, K., Kasza, K., Grier, D. G., *Sorting mesoscopic objects with periodic potential landscapes: Optical fractionation*. Physical Review E, 2004. **70**.
86. Xiao, K., Grier, D. G., *Sorting colloidal particles into multiple channels with optical forces: Prismatic optical fractionation*. Phys. Rev. E, 2010. **82**.
87. Faucheux, L.P., Bourdieu, L. S., Kaplan, P. D., Libchaber, A. J., *Optical thermal ratchet*. Phys. Rev. Lett., 1995. **74**.
88. Wong, W.P. and K. Halvorsen, *The effect of integration time on fluctuation measurements: calibrating an optical trap in the presence of motion blur*. Opt. Express, 2006. **14**: p. 12517-12531.
89. Crocker, J.C. and D.G. Grier, *Methods of digital video microscopy for colloidal studies*. Journal of Colloid and Interface Science, 1996. **179**: p. 298-310.
90. Jaquay, E., et al., *Light-Assisted, Templated Self-Assembly of Gold Nanoparticle Chains*. Nano Letters, 2014. **14**(9): p. 5184-5188.
91. Auguié, B. and W.L. Barnes, *Collective resonances in gold nanoparticle arrays*. Physical Review Letters, 2008. **101**: p. 143902.
92. Auguié, B., et al., *Diffraction arrays of gold nanoparticles near an interface: Critical role of the substrate*. Physical Review B, 2010. **82**: p. 155447.
93. Wong, H.M.K., et al., *On-a-chip surface plasmon tweezers*. Applied Physics Letters, 2011. **99**: p. 061107-3.
94. Slaughter, L.S., et al., *Toward Plasmonic Polymers*. Nano Letters, 2012. **12**: p. 3967-3972.
95. Edel, J.B., A.A. Kornyshev, and M. Urbakh, *Self-Assembly of Nanoparticle Arrays for Use as Mirrors, Sensors, and Antennas*. ACS Nano, 2013. **7**: p. 9526-9532.
96. Roxworthy, B.J., et al., *Plasmonic Optical Trapping in Biologically Relevant Media*. PLoS ONE, 2014. **9**: p. e93929.
97. Soltani, M., et al., *Nanophotonic trapping for precise manipulation of biomolecular arrays*. Nat Nano, 2014. **advance online publication**.

98. Al Balushi, A.A. and R. Gordon, *Label-Free Free-Solution Single-Molecule Protein–Small Molecule Interaction Observed by Double-Nanohole Plasmonic Trapping*. ACS Photonics, 2014. **1**: p. 389-393.
99. Yan, Z., et al., *Guiding Spatial Arrangements of Silver Nanoparticles by Optical Binding Interactions in Shaped Light Fields*. ACS Nano, 2013. **7**: p. 1790-1802.
100. Yan, Z., et al., *Hierarchical Photonic Synthesis of Hybrid Nanoparticle Assemblies*. Journal of Physical Chemistry Letters, 2013. **4**: p. 2630-2636.
101. Yan, Z., S.K. Gray, and N.F. Scherer, *Potential energy surfaces and reaction pathways for light-mediated self-organization of metal nanoparticle clusters*. Nature Communications, 2014. **5**: p. 4751.
102. Fan, S. and J.D. Joannopoulos, *Analysis of guided resonances in photonic crystal slabs*. Physical Review B, 2002. **65**: p. 235112.
103. Donner, J.S., et al., *Plasmon-assisted optofluidics*. ACS Nano, 2011. **5**: p. 5457-5462.
104. Mohanty, S., J. Andrews, and P. Gupta, *Optical binding between dielectric particles*. Optics Express, 2004. **12**: p. 2746-2753.
105. Johnson, P.B. and R.W. Christy, *Optical Constants of the Noble Metals*. Physical Review B, 1972. **6**(12): p. 4370-4379.
106. Hänggi, P. and F. Marchesoni, *Artificial Brownian motors: Controlling transport on the nanoscale*. Reviews of Modern Physics, 2009. **81**(1): p. 387-442.
107. Reimann, P., *Brownian motors: noisy transport far from equilibrium*. Physics Reports, 2002. **361**(2–4): p. 57-265.
108. Rousselet, J., et al., *Directional motion of Brownian particles induced by a periodic asymmetric potential*. Nature, 1994. **370**(6489): p. 446-448.
109. Faucheux, L., et al., *Optical thermal ratchet*. Physical Review Letters, 1995. **74**(9): p. 1504-1507.
110. Gorre-Talini, L., S. Jeanjean, and P. Silberzan, *Sorting of Brownian particles by the pulsed application of an asymmetric potential*. Physical Review E, 1997. **56**(2): p. 2025-2034.
111. Bader, J.S., et al., *DNA transport by a micromachined Brownian ratchet device*. Proceedings of the National Academy of Sciences, 1999. **96**(23): p. 13165-13169.
112. Hammond, R.W., et al., *Differential transport of DNA by a rectified Brownian motion device*. ELECTROPHORESIS, 2000. **21**(1): p. 74-80.
113. Huang, N., et al. *Light-assisted Templated Self-Assembly of a Gold Nanoparticle Array*. in *CLEO: 2014*. 2014. San Jose, California: Optical Society of America.
114. Chu, Y., Schonbrun, E., Yang, T. & Crozier, K. B., *Experimental observation of narrow surface plasmon resonances in gold nanoparticle arrays*. Applied Physics Letters, 2008. **93**: p. 181108.
115. Chu, Y., & Crozier, K. B., *Experimental study of the interaction between localized and propagating surface plasmons*. Optics Letters, 2009. **34**: p. 244-246.
116. Shahmansouri, A. and B. Rashidian, *Behavior of plasmonic nanoparticle array in near- and far-field coupling regimes for transverse electric and transverse magnetic polarizations*. Journal of the Optical Society of America B, 2013. **30**(8): p. 2286-2291.
117. Mock, J.J., et al., *Shape effects in plasmon resonance of individual colloidal silver nanoparticles*. The Journal of Chemical Physics, 2002. **116**(15): p. 6755-6759.
118. Ma, G., et al., *Self-Assembly Combined with Photopolymerization for the Fabrication of Fluorescence “Turn-On” Vesicle Sensors with Reversible “On–Off” Switching Properties*. Advanced Materials, 2006. **18**(1): p. 55-60.
119. Hillmyer, M.A., et al., *Self-assembly and polymerization of epoxy resin-amphiphilic block copolymer nanocomposites*. Journal of the American Chemical Society, 1997. **119**(11): p. 2749-2750.